UNIVERSIDADE ESTADUAL DE CAMPINAS
Faculdade de Engenharia Elétrica e de Computação

Lenin Patricio Jimenez Jimenez

About an UWB Social Distancing Monitoring System and a CA-CFAR Detector Performance Analysis over Weibull-Distributed Clutter Environments.

Sobre um Sistema de Monitoramento Social UWB e uma Análise de Desempenho de um Detector CA-CFAR operando em ambientes do tipo Weibull.

Campinas

2021

Lenin Patricio Jimenez Jimenez

About an UWB Social Distancing Monitoring System and a CA-CFAR Detector Performance Analysis over Weibull-Distributed Clutter Environments.

Sobre um Sistema de Monitoramento Social UWB e uma Análise de Desempenho de um Detector CA-CFAR operando em ambientes do tipo Weibull.

Thesis presented to the School of Electrical and Computer Engineering of the University of Campinas in partial fulfillment of the requirements for the degree of Master in Electrical Engineering, in the area of Telecommunications and Telematics.

Tese apresentada à Faculdade de Engenharia Elétrica e de Computação da Universidade Estadual de Campinas como parte dos requisitos exigidos para a obtenção do título de Mestre em Engenharia Elétrica, na área de Telecomunicações e Telemática.

Orientador: Prof. Dr. Gustavo Fraidenraich

Este trabalho corresponde à versão final da dissertação/tese defendida pelo aluno Lenin Patricio Jimenez Jimenez, e orientada pelo Prof. Dr. Gustavo Fraidenraich.

Campinas

2021

Ficha catalográfica
Universidade Estadual de Campinas
Biblioteca da Área de Engenharia e Arquitetura
Rose Meire da Silva - CRB 8/5974

J564a

Jimenez Jimenez, Lenin Patricio, 1995-
About an UWB social distancing monitoring system and a CA-CFAR detector performance analysis over Weibull-distributed clutter environments / Lenin Patricio Jimenez Jimenez. – Campinas, SP : [s.n.], 2021.

Orientador: Gustavo Fraidenracich.
Dissertação (mestrado) – Universidade Estadual de Campinas, Faculdade de Engenharia Elétrica e de Computação.

1. Distância social. 2. Monitoramento. 3. Covid-19. 4. Radar. 5. Rastreamento de destino. 6. Interferência de radar. I. Fraidenraich, Gustavo, 1975-. II. Universidade Estadual de Campinas. Faculdade de Engenharia Elétrica e de Computação. III. Título.

Informações para Biblioteca Digital

Título em outro idioma: Sobre um sistema de monitoramento social UWB e uma análise de desempenho CA-CFAR operando em ambientes do tipo Weibull
Palavras-chave em inglês:
Social distance
Monitoring
Covid-19
Tracking radar
Radar interference
Área de concentração: Telecomunicações e Telemática
Titulação: Mestre em Engenharia Elétrica
Banca examinadora:
Gustavo Fraidenraich
Michelle Soares Pereira Facina
André Saito Guerreiro
Data de defesa: 07-12-2021
Programa de Pós-Graduação: Engenharia Elétrica

Identificação e informações acadêmicas do(a) aluno(a)
- ORCID do autor: 0000-0002-0595-6509
- Currículo Lattes do autor: http://lattes.cnpq.br/3532452353797703

COMISSÃO JULGADORA - TESE DE MESTRADO

Candidato: Lenin Patricio Jimenez Jimenez RA: 264366
Data de defesa: 07 de Dezembro de 2021
Título da Tese: "Sobre um Sistema de Monitoramento Social UWB e uma Análise de Desempenho de um Detector CA-CFAR operando em ambientes do tipo Weibull."

Prof. Dr. Gustavo Fraidenraich (Presidente).
Dra. Michelle Soares Pereira Facina.
Dr. André Saito Guerreiro.

A Ata de Defesa, com as respectivas assinaturas dos membros da Comissão Julgadora, encontra-se no SIGA (Sistema de Fluxo de Dissertação/Tese) e na Secretaria de Pós-Graduação da Faculdade de Engenharia Elétrica e de Computação.

To my parents Ramiro and Lena, and to Cecilia.

Acknowledgements

First, to God for letting me achieve this challenge in my life.

To Prof. Gustavo, for allowing me to study at this prestigious University.

To my family and wife, for their love and support.

To Fernando Almeida, for the friendship, the guidance and valuable knowledge, he shared with me.

To my friends Gabriela, Byron, Diana, Karen, Levy, and Rony for bringing me their unconditional friendship during my stay in Brazil.

Finally, to Eduardo Rodrigues de Lima and Lucas Mendonca for all the support during my externship at Eldorado Research Institute.

This study was financed in part by the Coordenação de Aperfeiçoamento de Pessoal de Nível Superior - Brasil (CAPES) - Finance Code 001.

"If you want to find out about the road ahead, then ask about it from those coming back."

Chinese proverb

Resumo

Esta dissertação apresenta dois trabalhos realizados durante o meu mestrado. Em primeiro lugar, é apresentado um sistema de monitoramento de distanciamento social baseado na tecnologia Ultra Wideband (UWB) e, em segundo lugar, uma análise de desempenho do detector Cell Average Constant False Alarm Rate (CA-CFAR) sobre clutter do tipo Weibull.

O sistema de monitoramento do distanciamento social surge devido à pandemia Covid-19 e é executado em conjunto com o Instituto de Pesquisas Eldorado. Os principais elementos que compõem o sistema são *tags* e um *gateway*. As tags são dispositivos móveis carregados por pessoas como crachás de identificação. O gateway é um dispositivo fixo que coleta os dados gerados pelos usuários do tag. O sistema visa medir com alta precisão, $\leq$ 10 cm, distâncias entre pessoas. Ele registra informações de contato quando a distância entre duas ou mais pessoas é menor do que o permitido (ex. $\leq$ 1,50 m) e aciona um alerta sonoro para alertar as pessoas quando elas não estão respeitando o distanciamento social. Este sistema de monitoramento de distanciamento foi validado em um cenário real mostrando que o alerta sonoro aumenta a adesão a uma política de distanciamento social para 33 %.

A segunda contribuição está relacionada aos sistemas de radar e apresenta uma análise de desempenho do detector CA-CFAR sobre clutter do tipo Weibull. Para isso, são obtidas expressões novas e exatas para a probabilidade de detecção (PD) e a probabilidade de falso alarme (PFA). Ao contrário de trabalhos anteriores, as formulações propostas permitem que o parâmetro de forma assuma valores maiores ou iguais a um. Os resultados numéricos demonstram a importância de se considerar o valor correto do parâmetro de forma, uma vez que a detecção do radar melhora à medida que o parâmetro de forma aumenta.

Palavras-chaves: Distanciamento social; UWB; Detecção de radar; CA-CFAR.

Abstract

This dissertation presents two works carried out during my Master's. Firstly, it introduces a social distancing monitoring system based on Ultra Wideband (UWB), and secondly, a Cell Average Constant False Alarm Rate (CA-CFAR) detector performance analysis over Weibull distributed clutter.

The social distancing monitoring system arises due to the Covid-19 pandemic and is jointly executed with Research Institute Eldorado. The main elements composing the system are tags and a gateway. The tags are mobile devices carried by people as ID badges. The gateway is a fixed device that collects the data generated by the tag's users. The system aims to measure with high accuracy ($\leq$ 10 cm) distance between people. It records contact information when the distance between two or more people is less than allowed (ex.$\leq$ 1.50 m) and triggers an audible alert to warn people when they are not respecting the social distancing. This distancing monitoring system was validated in a real scenario showing that the audible alert increases the adherence to a social distancing policy to 33 %.

The second contribution is related to Radar systems and presents a CA-CFAR detector performance analysis over Weibull distributed clutter. To do so, novel and exact expressions for the probability of detection (PD) and probability of false alarm (PFA) are obtained. Unlike previous works, the proposed formulations allow the shape parameter to take values greater or equal than one. Numerical results demonstrate the importance of considering the right value of the shape parameter since radar detection improves as the shape parameter increase.

Keywords: Social-Distancing; UWB; Radar-Detection; CA-CFAR..

List of Figures

—

List of Tables

List of Acronyms

SARS-CoV-2	severe acute respiratory syndrome coronavirus 2
UWB	ultra wide band
GPS	global positioning system
Wi-Fi	wireless fidelity
ECMA	European Computer Manufacturers Association
TWR	two way ranging
Tx	transmitter
Rx	receiver
ITU	International Telecommunications Union
CFAR	constant false-alarm rate
CA-CFAR	cell averaging constant false-alarm rate
GO-CFAR	greatest of constant false-alarm rate
SO-CFAR	small of constant false-alarm rate
OR-CFAR	ordered statistic constant false-alarm rate
ML-CFAR	maximum-likelihood constant false-alarm rate
PDF	probability density function
CDF	cumulative distribution function
CUT	cell under test
NP	Neyman-Pearson
PD	probability of detection
PFA	probability of false alarm
MC	Monte Carlo
ROC	receiver's operating characteristic
RV	random variable
SNR	signal-to-noise ratio
SCR	signal-to-clutter ratio

List of Symbols

$\Gamma(\cdot)$	gamma function
$\Gamma(\cdot,\cdot)$	upper incomplete gamma function
$\gamma(\cdot,\cdot)$	lower incomplete gamma function
$f_Z(\cdot)$	probability density function of a generic random variable Z
$F_Z(\cdot)$	cumulative distribution function of a generic random
$\Pr[\cdot]$	probability of an event
$\mathbb{E}[\cdot]$	expectation
$\lvert\cdot\rvert$	absolute value

List of Publications

Journal Article

- L. Jimenez, F. D. A. García, M. C. Luna, E. R. de Lima and G. Fraidenraich, "A General CA-CFAR Performance Analysis for Weibull-Distributed Clutter Environments," *IEEE Geosci. Remote Sens. Lett*, under review, 2021.

Conference Article

- Jimenez L., de Lima E.R., Fraidenraich G. (2022) Social Distancing Experiment Based on UWB Monitoring System. In: Ahram T., Taiar R. (eds) Human Interaction, Emerging Technologies and Future Systems V. IHIET 2021. Lecture Notes in Networks and Systems, vol 319. Springer, Cham. https://doi.org/10.1007/978-3-030-85540-6_131

Co-Authored Journal Articles

- M. C. Luna, F. D. A. García, L. Jimenez, G. Fraidenraich and Y. Iano. "Performance Evaluation of SOCA-CFAR Detectors in Weibull-Distributed Clutter Environments," *IEEE Geosci. Remote Sens. Lett*, under review, 2021.

Contents

1 UWB Social Distancing Monitoring System

This chapter is based on the paper below:

- Jimenez L., de Lima E.R., Fraidenraich G. 2022 Social Distancing Experiment Based on UWB Monitoring System. In: Ahram T., Taiar R. (eds) Human Interaction, Emerging Technologies and Future Systems V. IHIET 2021. Lecture Notes in Networks and Systems, vol 319. Springer, Cham. https://doi.org/10.1007/978-3-030-85540-6_131

1.1 Introduction

The severe acute respiratory syndrome coronavirus 2 (SARS-CoV-2) pandemic caught the world off guard. It is difficult to quantify the real impact that the pandemic had both on society and the global economy. Studies showed, in terms of statistics, the devastating impact of the pandemic. For example, [1] confirms that for the first time, since 1990, global poverty could increase, and [2] affirms that 25 million jobs could be lost as a result of Covid-19. In [3], authors present a complete study about the pandemic impact in fields such as the petroleum industry, education, manufacturing industry and travel industry. It reveals that in March 2020 the petroleum industry registered the lowest value for an oil barrel in the last 30 years. Another field that was ravaged is education. It is estimated that 900 million students worldwide were affected for different reasons due to the pandemic.

Likewise, due to the pandemic, the manufacturing industry and sectors, where remote work is not viable, have experienced many challenges, two of these were: to increase sanitation measures to guarantee the employee's well-being in workplaces that are typically dense and, to control possible outbreaks of Covid-19 in case anyone gets infected. The World Health Organization published a list of recommendations to help contain the spread of the virus [4]. Among them, we have the mandatory use of masks, the periodic cleaning of hands with alcohol or soap and water, the periodic sanitation of workplaces, to maintain at least a 1-meter distance between people, daily temperature checks and, people's self-isolation if symptoms are present. In addition, the Center for Disease Control and Prevention recommends interactions between people don't exceed a maximum cumulative time duration of 15 minutes [5]. In this context, we propose in this chapter a social distancing monitoring system to help avoid and contain possible outbreaks. The system aims to measure with high precision the distance between people, to warn the users with a real-time audible or visible alert when they break the social distancing policy, and to record the events when the users break the social distancing policy.

This chapter also analyzes the behavior of a group of people using an UWB-based social distancing monitoring system. This social experiment shows that despite the implementation of protection measures and the proper signaling to keep social distance, people tend to disrespect social distancing. The main contributions of this chapter are:

1. The deployment of an UWB-based social distancing monitoring system in an industrial scenario, taking real measurements of people's behavior.

2. The implementation of a four-stage methodology in the experiment to quantify the real impact of the monitoring system. In each stage, the volunteers receive a certain level of information starting with a zero-knowledge about the experiment and ending with a personal real-time warning when the social distancing policy is broken.

3. The correct processing of the collected data to generate a log of contact between people. This allows generating an early and fast people isolation protocol in case of infection based on real data.

The remainder of this chapter is organized as follows. Section 1.2 gives a comparison with related works. Section 1.3 introduces main concepts about UWB technology. Section 1.4 presents the elements and features of the social distancing monitoring system. Section 1.5 describes the experiment that was carried out including the obtained results. Finally, in section 1.6 a general conclusion is presented.

1.2 Related works

As soon as the virus spread began around the world, many fields of science got involved in different studies to create mechanisms that will help contain it [6, 7, 8, 9, 10, 11]. As for technological solutions related to proximity monitoring, numerous alternatives were proposed. For example, in [12] the authors present a solution based on computational vision and machine learning. To obtain high precision distance measurements a camera is used. The downside of this approach is that the precision of the measured distance (between people) is inversely proportional to the distance between the persons and the camera. The system's lack of portability is another disadvantage since it is limited to cover the fixated area where the camera is deployed. Likewise, authors in [13] benefits from computational vision to develop a system that counts the number of people and measures the distance between them using face recognition. The system triggers an alert via SMS if/when the capacity of an area is exceeded. As in [12], the same weakness is observed.

Further related works make use of wireless technologies such as: Bluetooth, GPS, Wi-Fi, and UWB. For example, [14] proposes a wearable device that uses Bluetooth and Wifi. The work introduces a system that uses color LEDs to signal people. The colors green, yellow and red state for safe, mildly suspicious, and highly suspect respectively. At first, for all users, the wearable device indicates green and could later change if they had contact (for a certain period of time) with a suspect or a confirmed case. The distance measure between users is done via Bluetooth. The report of new cases and color variations is done via Wi-Fi to a server. The downside of this system is the low precision in distance measurement that Bluetooth offers in addition to employing an extra Wi-Fi module that derives into a battery-hungry device. In [15] authors propose a mobile app using Bluetooth to measure social distancing. In this case, a push notification is emitted if two people don't follow the social distance policy. The main disadvantage here is the need for special permissions to link multiple mobile devices via Bluetooth, which can risk the personal data of each user. In [16] an UWB device is presented. The wearable device measures, with high precision, social distancing. The device generates an audible and visible alert to

warn people when they are not adhering to the distancing policies. Although the system is innovative, it does not have a subsystem that generates a contact trace log between people which, can become handy when tracing interactions between people in case of a possible infection. Finally, in [17, 18] the authors presented a complete overview of technologies and techniques used for indoor localization and social distancing where parameters such as accuracy, energy efficiency, and latency are compared.

1.3 UWB technology - Brief description

UWB wireless communication technology is characterized by a high bandwidth ($\geq$ 500 MHz) [19]. The standard for UWB communications was published in the IEEE 802.15.4a release (i) where the UWB physical layer was added [20]. UWB communications have by far the largest allocation of bandwidth, see Figure 1.1. For example, the US Federal communication Commission (FCC) allocates 7.5 GHz of band between 3.1 [GHz] and 10.6 [GHz] with a restriction power available to a transmitter, near to 0.5 [mW] [21]. In 2008 the European Computer Manufacturers Association (ECMA) specifies in its ECMA-368 a multiband-OFDM system that divides the frequency spectrum into 14 bands and 6 band groups as shown in Figure 1.2. Each one has 528 [MHz] of bandwidth [22].

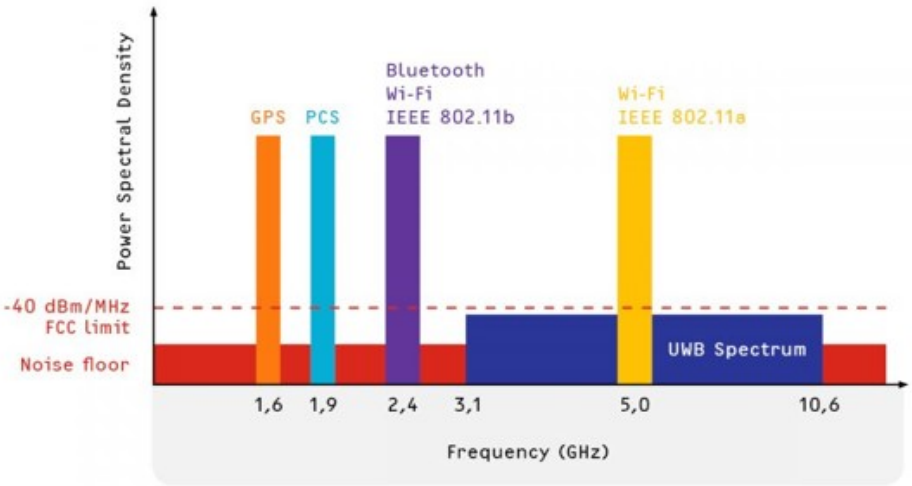

Figure 1.1 – UWB spectrum *vs* other wireless technologies.

UWB is classified as a pulse modulation technique. This pulse can directly propagate in the radio channel without the need of an additional carrier modulation. The carrier-less architecture of the impulse radio UWB facilitates the development of low-power transmitters and receivers [21]. Other important features of UWB are:

(i) Have a noise-like signal spectrum;

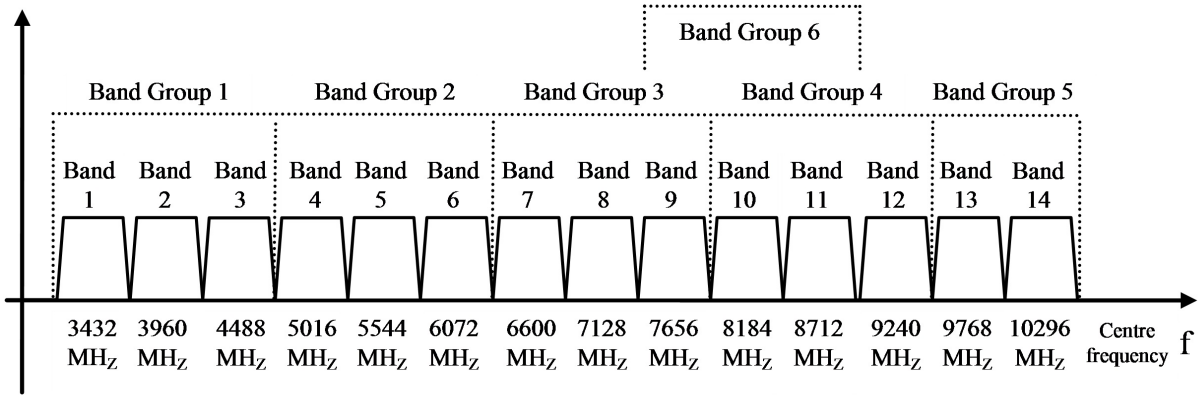

Figure 1.2 – UWB frequency bands.

(ii) To be resistant to severe multipath and jamming;

(iii) Have a good time-domain resolution allowing for positioning and proximity applications.

The ranging applications in UWB are based on the two-way ranging (TWR) protocol. The TWR protocol is a handshake that collects distance information by estimating the round-trip time of signals in the free space [20]. Figure 1.3. gives a better understanding of how the protocol works. There are two devices, the transmitter (Tx) and the receiver (Rx), in a ranging process. The Tx begins sending a range request packet to the Rx. Then Rx sends back a confirmation link packet. The distance between Tx and Rx can be easily calculated by the product between the velocity of light and the time spent in the packets exchange. If the distance between Rx and Tx is of interest an extra packet from Tx must be sent [21]. To guarantee the well functioning of a system based on this protocol, the number of tags must be lower than 20. If the number of tags is greater, a protocol to avoid packets collision must be implemented.

1.4 System overview

The social distance monitoring system is composed of two main devices: the tags and the gateway. The tags are mobile devices that create a mesh-type network where each device communicates via UWB with the other tags. The gateway is a fixed element that fulfills the function of a data collector. Figure 1.4 gives a general view of the system´s architecture. A detailed description of each element is described below.

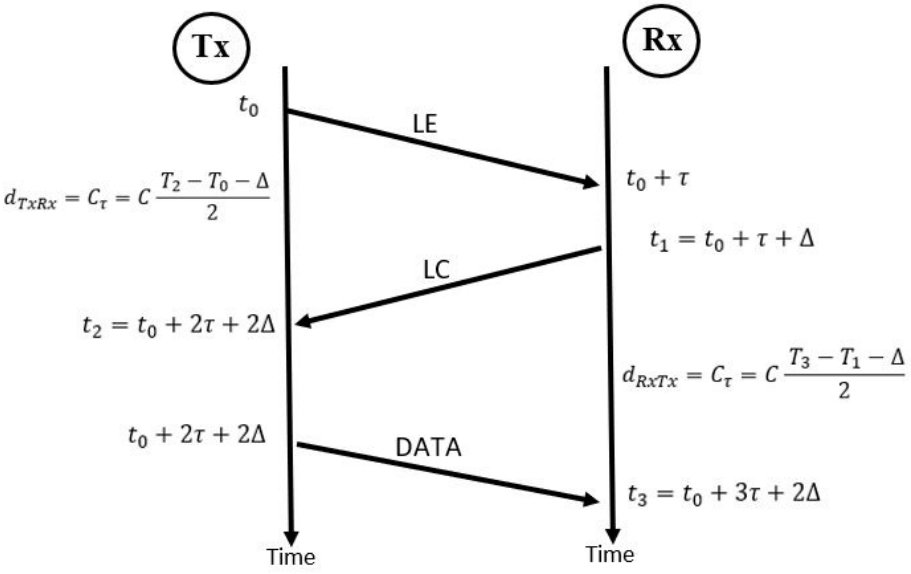

Figure 1.3 – Two-way ranging protocol.

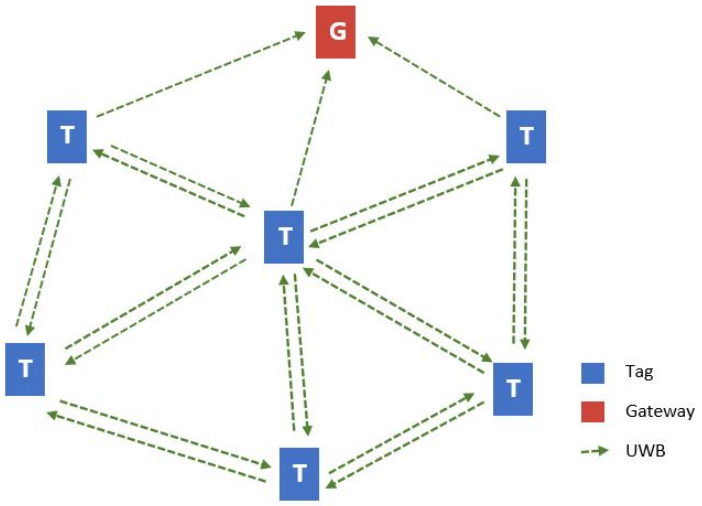

Figure 1.4 – Distancing monitoring system topology.

1.4.1 Tags

A tag is an electronic device worn by users as an ID badge, as shown in Figure 1.5. The device is an UWB radio based on a DW1001c chip. It has a 700 [mAh] battery that guarantees five operating hours. It runs an UWB multi-range software, developed by our project partners RTLOC, that allows distance measurement from 1 up to 20 devices simultaneously. Other features of this gadget are:

(i) Its dimensions are 12 cm x 6 cm x 2.5 cm;

(ii) Contains an adapted buzzer to emit an audible alert;

(iii) Posses a unique alphanumeric ID;

Figure 1.5 – Tag worn by a participant.

(iv) Stores the ID, the time-lapse, and the date of the event. An event occurs when the distance between two or more devices is less than 1.5 [m];

(v) Downloads the stored data to the gateway via UWB.

The tag operation is described as follows: First, each tag continuously transmits a pulse. Between transmissions, the tag listens for UWB pulses emitted by other tags. When an incoming pulse is detected, the distance between the devices is calculated by a package exchange based on the TWR protocol. If the calculated distance is less than the allowed, two concurrent processes start in the device. The first one is an audible and/or visible alert that the tag emits to warn the user about the proximity with another person. The second is storing the following parameters: ID, time-lapse, and timestamp when an event occurs. Both processes finalize when the devices move apart into a "safe" distance. Finally, the tag downloads the stored data when passing near the gateway.

1.4.2 Gateway

The gateway is a fixed element configured as a listener, i.e., it does not emit any kind of response, it is limited to collecting data from the tags. It is possible to get the tag´s data via Bluetooth or via UWB. The main difference between these two approaches is the download speed. A test performed with a Bluetooth gateway showed a download speed of an event per second while, with an UWB gateway, the download speed was 10 events per second. Due to the huge difference in the download speed, only the UWB gateway was considered.

The UWB gateway's connection is presented in Figure 1.6. The gateway communicates via UWB with the tags and via Ethernet to a local area network (LAN) where a computer is listening and saving the data of each tag.

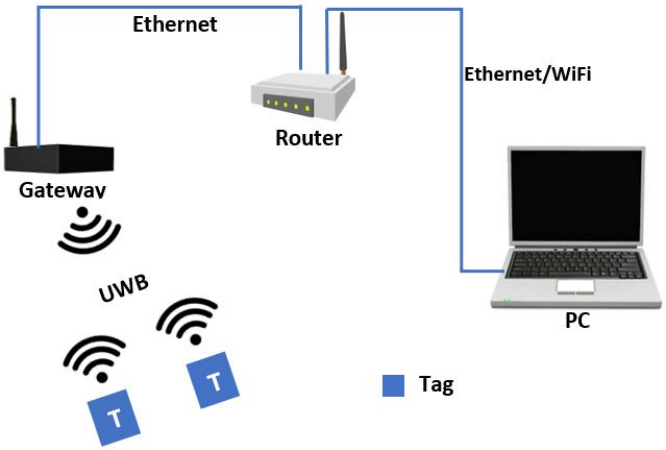

Figure 1.6 – Gateway connection diagram.

The collected data is stored in a text file. The text file contains the tag's events, and each event is represented in two frames. The structure of the frames is shown in Table 1.1. The first parameter corresponds to the number of the event (NE). The second indicates the type of frame (I/O). Type 1 represents the entry of the tag to a non-safe zone and type 2 is the exit of the tag to a safe zone. The third (ID1) is the tag's ID and the fourth parameter (ID2) is the ID with whom the tag had contact. The fifth parameter (AD) is the allowed set distance. MD represents the minimum distance between the tags during the event. TD is the time duration, in seconds, of the event. The last parameter (DATE) indicates the date (year, month, day, hour, minute, and second) in epoch format of when the event occurred.

Table 1.1 – Event data frames structure.

NE:	**I/O:**	**ID1:**	**ID2:**	**AD:**	**MD:**	**TD:**	**DATE:**
25	1	23967	39211	150	0	0	11259050792912869
26	2	23967	39211	150	118	13	12947900653176805

Once all the events are stored in the PC, an algorithm is executed to generate statistics about the users' behavior during the day. The algorithm follows the flowchart presented in Figure 1.7. The raw data and the participants' list are the entries of the algorithm. The participants list is a file that relates the ID of each tag with the name and e-mail of each participant. The raw data is filtered by date to bound the events for a day, then is cleaned and ordered. After that, the total number of events is calculated. Then the events are joined in terms of interactions. An interaction means the time duration cumulative sum of different events with the same participant, i.e., is possible to have many events with the same person but at the end of the day, all the events with that person are summed and represented as an interaction. Once the data is in terms of interactions, some interesting statistics such as the percentage of not adherence to the distancing

policy and the distribution according to the time duration of the interactions are obtained. The algorithm ends by sending via e-mail the statistics to all the participants and, if an interaction of any of the participants had registered a cumulative time duration greater than 15 minutes during the day a personal e-mail notification to the participant is sent.

1.5 The experiment

In order to quantify the impact of the distancing monitoring system on people's behavior, an experiment was performed. The experiment was carried out for 4 days, one stage per day. The participants belong to one of the departments of a company. The place was well signposted to warn about social distancing. Also, self-care tips were posted in common areas and the use of the mask was mandatory.

The experiment consisted of analyzing the behavior of 15 people employing a UWB monitoring system with a specific tag configuration in each stage. The experiment measured the number of times the individuals broke the social distance policy which consisted of standing near another person at a distance of fewer than 1.5 meters for more than 20 seconds. Each day, when the users register their entry in the morning, a tag was given to them. After they finish their working day, the tag was given back. Also, it is important to mention that during this experiment, no group nor personal e-mails were sent. Further details and the different tag configurations used on each day of the experiment are described below.

1.5.1 Day 1: No feedback

On the first day the tags were configured in silence mode, i.e, the devices do not emit any kind of alert if an event occurs. The only instruction that was given to the users was always to carry the tag with them. The data generated in the 15 tags was later collected by the gateway and processed to obtain the first results.

1.5.2 Day 2: It is an experiment due to SARS-CoV-2

On the second day, the tag was again configured in silence mode. Unlike day 1, it was explained to volunteers that the devices (tags) are part of an experiment that aims to measure their proximity with their coworkers due to the SARS-CoV-2 pandemic. At the end of the working day, the tags were returned, and all the collected data was processed.

1.5.3 Day 3: Look how you are behaving

The data obtained from day 2 was presented to the users as visual feedback. It consisted of two pie charts that showed them the adherence percentage of the social

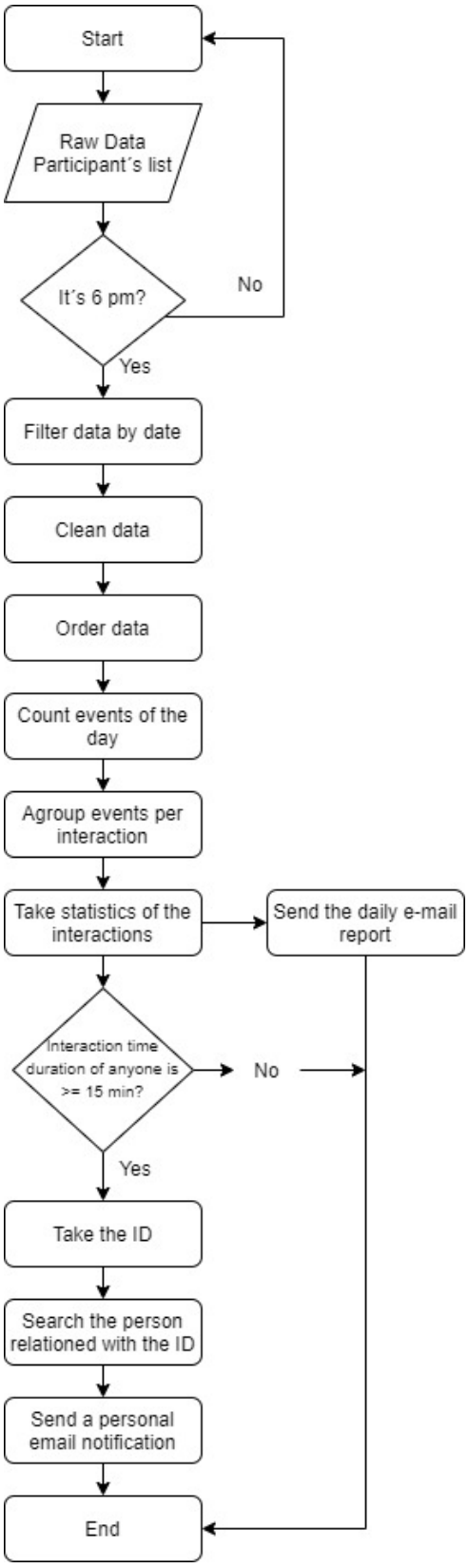

Figure 1.7 – Data processing flow chart.

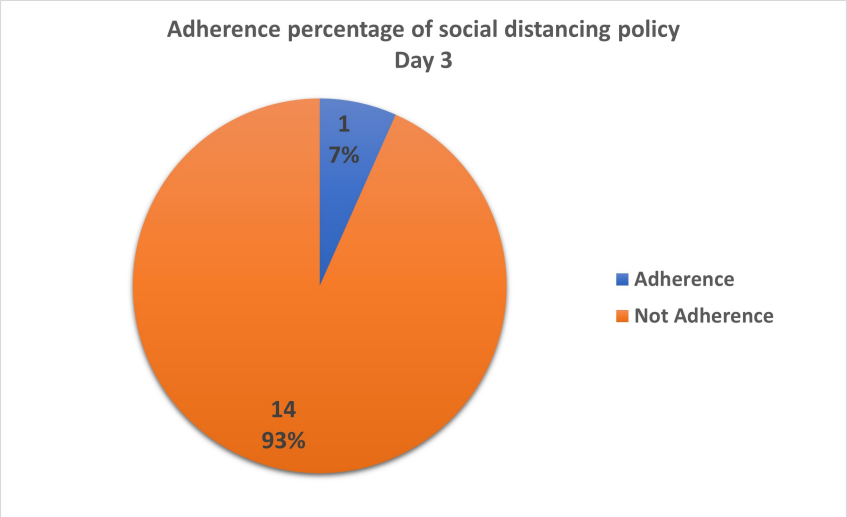

Figure 1.8 – Adherence percentage on the third day.

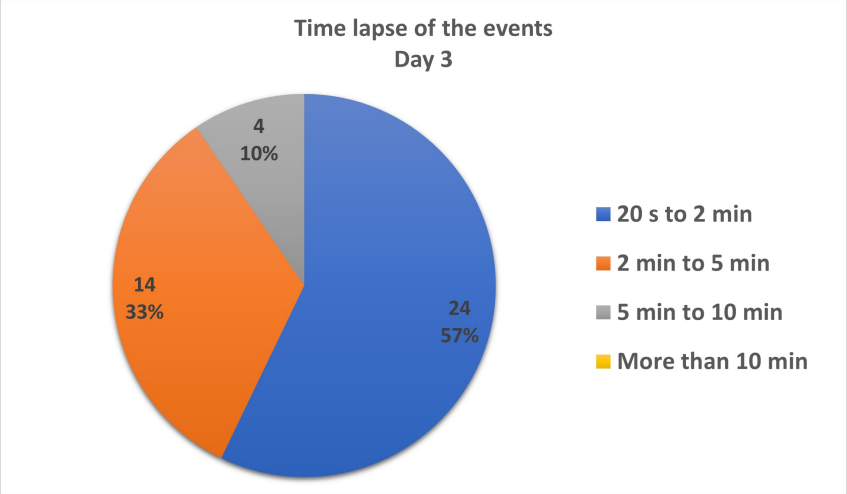

Figure 1.9 – Time-lapse of the events on the third day.

distancing policy and the distribution of the events according to the time-lapse, see Figure 1.8 and Figure 1.9. This was done in order to observe their responses (conduct during the day), having prior knowledge of their general behavior. The tags were also configured in silence mode and the data was collected in the same way.

1.5.4 Day 4: A personal feedback

As in day 3, the results of the previous day were presented in a pie chart in order to provide a feedback to the persons. The tags were not configured in silence mode, the adapted buzzers of the devices were to emit an audible alert in case of occurrence of an infraction of the policy. The volume of the audible alert was regulated so it would not disturb the people. The results of this day were collected and processed for further analysis.

1.5.5 Results of the experiment

After performing a careful analysis of the acquired data, the following results were obtained. Figure 1.10 shows the adherence and non-adherence percentage to the social distancing policy presented by the users per day. In days 1, 2, and 3 the non-adherence percentage is much more significant (having values that are greater than 80%), meaning that the social distance policy was not followed at all. On the fourth day, the non-adherence percentage dropped to 67% which can be attributed to the audible alert and represents a slight improvement. However, even though the volunteers had the knowledge (from day 2) that the experiment consisted of social distancing and even with audible alerts, the percentage of non-adherence is quite high (more than 50%).

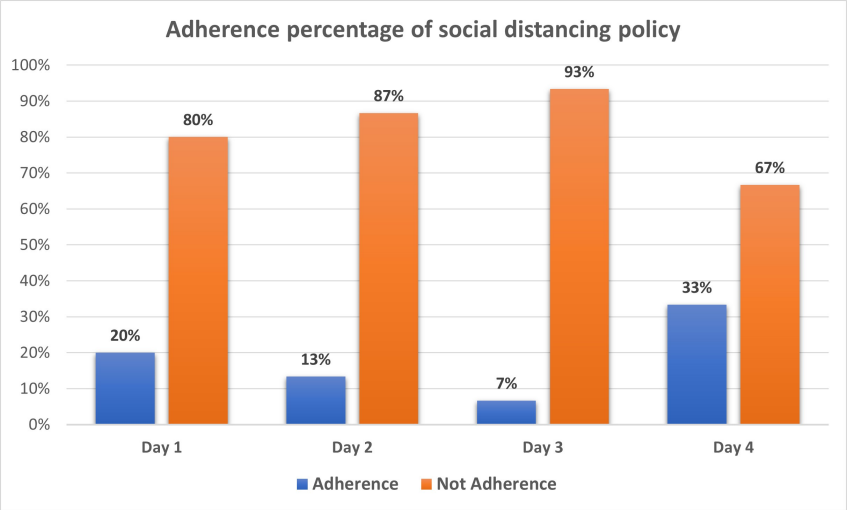

Figure 1.10 – Adherence percentage of social distancing policy per day.

Another relevant information obtained through the collected data is the number of events per day, i.e. how many times the social distancing policy was broken. This behavior is illustrated in Figure 1.11. In the first two days we encountered a similar number of infringements. Considering that 15 people are part of the experiment we can infer that 80% of the users broke the social distance policy at least once. As for the third day, there is a significant increase in the number of events. Considering that, at the time, the users already known their role in the experiment and taking into account the feedback that was given to them, it was expected that the number of events would at least be maintained if not diminished. The number of events during the third day suggests a further analysis of the data. Activities that were not contemplated, such as a department meeting, could demand a group interaction and may justify the number of events. On the fourth day, the number of events drastically dropped to 15. As mentioned before, this could be attributed to the audible alert people hear whenever an event occurs.

As mentioned earlier, the system could be useful to help implement isolation protocols in case of an infection. To exemplify this feature, suppose the subject “06A”

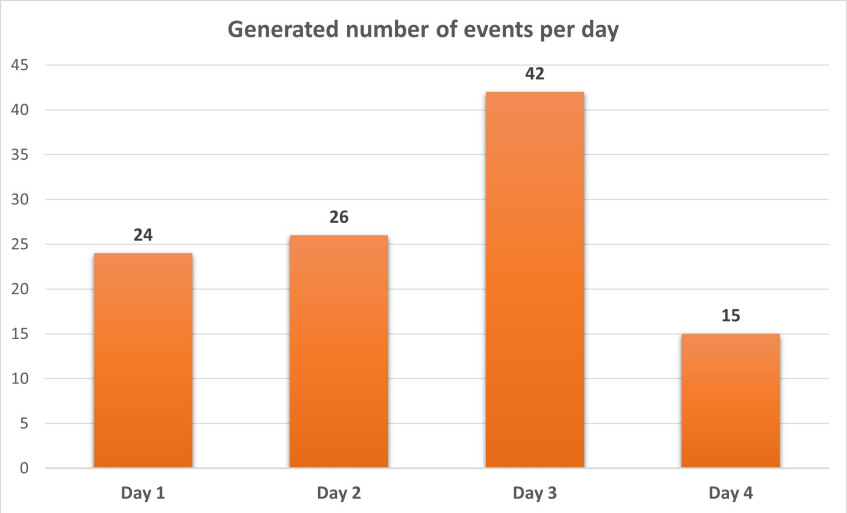

Figure 1.11 – Number of events per day.

Tag ID	191C	C9B1	01B5	9234	52A4	9399	8092	CA82	1200	D9A8	D90D	5B35	06AC	901E	0C38
191C	0	0	0	0	0	0	0	0	0	401	22	0	0	0	57
C9B1	0	0	0	0	0	0	0	0	22	0	0	0	0	0	0
01B5	0	0	0	0	0	0	0	0	0	0	0	0	0	0	0
9234	0	0	0	0	0	0	0	0	23	0	0	426	260	0	0
52A4	0	0	0	0	0	0	0	25	0	0	0	0	0	26	0
9399	0	0	0	0	0	0	0	0	0	0	0	0	0	0	0
8092	0	0	0	0	0	0	0	0	0	166	109	0	0	0	0
CA82	0	0	0	0	25	0	0	0	0	0	0	0	0	0	0
1200	0	22	0	23	0	0	0	0	0	0	0	0	21	0	0
D9A8	400	0	0	0	0	0	167	0	0	0	0	0	0	0	828
D90D	23	0	0	0	0	0	109	0	0	0	0	0	0	21	0
5B35	0	0	0	426	0	0	0	0	0	0	0	0	422	0	0
06AC	0	0	0	260	0	0	0	0	0	0	0	425	0	0	0
901E	0	0	0	0	26	0	0	0	0	0	22	0	0	0	0
0C38	58	0	0	0	0	0	0	0	0	828	0	0	0	0	0

Figure 1.12 – Tracking example of supposed SARS-CoV-2 case.

has tested positive for SARS-CoV-2. The data collected by the tags allows to track every contact the person has had with his/her coworkers during the past days. As shown in Figure 1.12, the user “06AC” interacted with users “9234” and “5B35” for a period of 260 [s] and 425 [s] respectively. Similarly, the interaction of users “9234” and “5B35” can be tracked down. This allows for rapid response as well as for isolation protocols and, thereby prevents the increase of infectious cases.

1.6 Conclusion

A functional distancing monitoring system was implemented and validated in a real scenario experiment. The data obtained during the experiment showed how the adherence percentage of the social distancing policy does not increase much even if the place has the proper signaling, indirect warn messages like self-care posters are showed, and direct warning messages like statistics about their behavior are presented. It is also showed that personal real-time feedback (the buzzer) helps to increase the adherence percentage of the social distancing policy by 20% in the experiment. Finally, the system is useful to control a possible outbreak due to the implemented contact data matrix.

1.7 Bibliography

[1] M. Buheji, K. Cunha, and B. Mavrić, "The extent of covid-19 pandemic socio-economic impact on global poverty. a global integrative multidisciplinary review," *American Journal of Economics*, vol. 10, pp. 213–224, 04 2020.

[2] I. L. Organization. Almost 25 million jobs could be lost worldwide as a result of covid-19. 2020, March 18. [Online]. Available: https://www.ilo.org/global/about-the-ilo/newsroom/news/WCMS_738742/lang--en/index.htm

[3] M.Nicola, Z. Alsafi, C.Sohrabi, and A.Kerwan, "The socio-economic implications of the coronavirus pandemic (covid-19): A review." *International journal of surgery (London, Englan*, 04 2020.

[4] W. H. Organization. "Advice for the public". (2020, March 10). [Online]. Available: https://www.who.int/emergencies/diseases/novel-coronavirus-2019/advice-for-public

[5] Centers for Disease Control and Prevention (CDC). "COVID-19 Glossary of Key Terms". (2021, Oct. 11). [Online]. Available: https://www.cdc.gov/coronavirus/2019-ncov/php/contact-tracing/contact-tracing-plan/appendix.html#contact

[6] J. Kudela, "Social distancing as p-dispersion problem," *IEEE Access*, vol. 8, pp. 149 402–149 411, 2020.

[7] A. S.-E. H. Hao-Yuan Cheng, "Proactive and blended approach for covid-19 control in taiwan," *Biochemical and Biophysical Research Communications*, 2020.

[8] T. Amano, H. Yamaguchi, and T. Higashino, "Connected ar for combating covid-19," *IEEE Internet of Things Magazine*, vol. 3, no. 3, pp. 46–51, 2020.

[9] A. A. R. Alsaeedy and E. K. P. Chong, "Detecting regions at risk for spreading covid-19 using existing cellular wireless network functionalities," *IEEE Open Journal of Engineering in Medicine and Biology*, vol. 1, pp. 187–189, 2020.

[10] P. He, "Study on epidemic prevention and control strategy of covid -19 based on personnel flow prediction," in *2020 International Conference on Urban Engineering and Management Science (ICUEMS)*, 2020, pp. 688–691.

[11] R. Sethi, M. Mehrotra, and D. Sethi, "Deep learning based diagnosis recommendation for covid-19 using chest x-rays images," in *2020 Second International Conference on Inventive Research in Computing Applications (ICIRCA)*, 2020, pp. 1–4.

[12] S. Gupta, R. Kapil, G. Kanahasabai, S. S. Joshi, and A. S. Joshi, "Sd-measure: A social distancing detector," in *2020 12th International Conference on Computational Intelligence and Communication Networks (CICN)*, 2020, pp. 306–311.

[13] S. Rajarajeshwari, S. Archana, S. R. Boda, R. B. Sreelakshmi, K. Venkateswaran, and N. Sridhar, "A smart image processing system for hall management including social distancing - "sodiscop"," in *2020 Third International Conference on Smart Systems and Inventive Technology (ICSSIT)*, 2020, pp. 1213–1219.

[14] A. K. Tripathy, A. G. Mohapatra, S. P. Mohanty, E. Kougianos, A. M. Joshi, and G. Das, "Easyband: A wearable for safety-aware mobility during pandemic outbreak," *IEEE Consumer Electronics Magazine*, vol. 9, no. 5, pp. 57–61, 2020.

[15] M. E. Rusli, S. Yussof, M. Ali, and A. A. Abobakr Hassan, "Mysd: A smart social distancing monitoring system," in *2020 8th International Conference on Information Technology and Multimedia (ICIMU)*, 2020, pp. 399–403.

[16] Y. Cao, A. Dhekne, and M. Ammar, "6fit-a-part: A protocol for physical distancing on a custom wearable device," in *2020 IEEE 28th International Conference on Network Protocols (ICNP)*, 2020, pp. 1–12.

[17] C. T. Nguyen, Y. M. Saputra, N. V. Huynh, N. T. Nguyen, T. V. Khoa, B. M. Tuan, D. N. Nguyen, D. T. Hoang, T. X. Vu, E. Dutkiewicz, S. Chatzinotas, and B. Ottersten, "A comprehensive survey of enabling and emerging technologies for social distancing—part i: Fundamentals and enabling technologies," *IEEE Access*, vol. 8, pp. 153 479–153 507, 2020.

[18] F. Zafari, A. Gkelias, and K. K. Leung, "A survey of indoor localization systems and technologies," *IEEE Communications Surveys Tutorials*, vol. 21, no. 3, pp. 2568–2599, 2019.

[19] B. Großwindhager, C. A. Boano, M. Rath, and K. Römer, "Concurrent ranging with ultra-wideband radios: From experimental evidence to a practical solution," in *2018 IEEE 38th International Conference on Distributed Computing Systems (ICDCS)*, 2018, pp. 1460–1467.

[20] E. Karapistoli, F. Pavlidou, I. Gragopoulos, and I. Tsetsinas, "An overview of the ieee 802.15.4a standard," *IEEE Communications Magazine*, vol. 48, no. 1, pp. 47–53, 2010.

[21] M.-G. D. Benedetto, *UWB communication systems: a comprehensive overview*. Hindawi Publishing Corporation, 2006.

[22] ECMA, *High Rate Ultra Wideband PHY and MAC Standard*, Std., dec 2008.

2 CA-CFAR Performance Analysis for Weibull-Distributed Clutter Environments

This chapter is based on the paper below:

- L. Jimenez, F. D. A. García, M. C. Luna, E. R. de Lima and G. Fraidenraich, "A General CA-CFAR Performance Analysis for Weibull-Distributed Clutter Environments," *IEEE Geosci. Remote Sens. Lett*, under review, 2021.

Note: The following chapter is related with radar detection theory. The text presented below is totally independent of chapter 1.

2.1 Introduction

Due to the random characteristics of noise and interference, radar performance is evaluated in terms of probabilities, namely, probability of detection (PD) and probability of false alarm (PFA). A detection is declared whenever the received signal surpasses a fixed threshold [1, 2, 3]. In scenarios where the interference is too strong (common in practice), using a fixed threshold will contribute to an increase in the false alarm rate. In such scenarios, constant false alarm rate (CFAR) detectors are often used. In general, CFAR detectors seek to maintain a fixed rate of false alarms by adaptively modifying their detection thresholds [4].

Different CFAR detectors have been introduced in the literature. Among the most common, we highlight the cell-averaging CFAR (CA-CFAR), the smallest-of CFAR (SOCA-CFAR), the greatest-of CFAR (GOCA-CFAR), the ordered statistic CFAR (OS-CFAR), and the maximum-likelihood CFAR (ML-CFAR) [5, 6, 7, 8]. The main difference between CFAR detectors is how they built the statistical functions of their systems. For instance, CA-CFAR detectors set the threshold by averaging the interference samples within the CFAR window [1, 9].

Clutter is one of the interfering signals that most degrades a radar system. Due to its nature, clutter is commonly characterized by its probability density function (PDF) or cumulative distribution function (CDF). The most used statistical models to describe clutter's behavior are the ones that exhibit longer tails such as Log-Normal, Gamma, Weibull, and K distributions [10, 11, 12]. Notably, the Weibull distribution has proved to be an excellent fit to model both ground and sea clutter [13, 14, 15]. Therefore, it is imperative to analyze radar performance under this type of clutter interference.

It is well known that when dealing with Weibull clutter in CFAR detectors the mathematical development is complex, starting from: i) the sum statistics of the clutter samples contained in the CFAR window, up to ii) the sum statistics for the target-plus-clutter samples within the cell under test (CUT). To simply the cumbersome maths, most works fix the value of the Weibull's distribution shape parameter to one or two resulting in exponentially or Rayleigh-distributed clutter, respectively [14, 15, 16, 17, 18, 19, 20, 21, 22, 23, 24]. For instance, in [20] the authors analyzed the performance of a CA-CFAR detector by deriving an accurate approximation for the PD and an exact solution for PFA. To do so, they considered arbitrary values for the shape parameter of the clutter samples within the CUT. Nonetheless, the shape parameter of the clutter samples contained in the CFAR window was set to two (i.e., Rayleigh clutter). Recently, in [21], considering arbitrary

values for the shape parameter of the Weibull interference, the authors obtained the exact sum statistics for the target-plus-clutter sample within the CUT and then derived the corresponding performance metrics (i.e., PD and PFA). However, no CA-CFAR analysis was carried out in that work. To the best of the author's knowledge, there are no exact performance analyses for a CA-CFAR detector considering arbitrary values for the shape parameter in both the CUT and the CFAR window.

In this chapter, capitalizing on [25] and proposing alternative exact solutions for the CUT's statistics, we derive the corresponding performance metrics for a CA-CFAR detector working over homogeneous Weibull-distributed clutter. For the analysis, we allow the shape parameter of the Weibull clutter to take values greater than or equal to one (regime of paramount importance in many practical applications) in both the CUT and the CFAR window.

It is worth mentioning that the proposed methodology can also be used to analyze the general performance of more robust CFAR detectors, such as SOCA-CFAR, GOCA-CFAR, and ML-CFAR.

The remainder of this chapter is organized as follows. Section 2.2 presents basic concepts related to Radar theory. Section 2.3.2 introduces the system model as well as the statistics for the CUT and CFAR window. Section 2.3.3 derives the generalized expressions for PFA and PD of a CA-CFAR detector. Section 2.3.4 presents the numerical results and validates the obtained expressions. Finally, Section 2.4 summarizes the main conclusions.

In what follows, $f_{(\cdot)}(\cdot)$, denotes PDF; $F_{(\cdot)}(\cdot)$, CDF; $\Gamma(\cdot)$, the gamma function [26, eq. (6.1.1)]; $\gamma(\cdot\,,\cdot)$, the lower incomplete gamma function [26, eq. (6.5.2)]; $\Gamma(\cdot\,,\cdot)$, the upper incomplete gamma function [26, eq. (6.5.3)]; $\mathbb{E}\left[\cdot\right]$, expectation; and $|\cdot|$, absolute value.

2.2 Theoretical Background

In this section important concepts that give a better understanding of this chapter are presented.

2.2.1 Radar concepts

A basic radar can be defined as a device that emits radio waves to detect an object and determine its position [27]. The word radar is derived from *radio detection and ranging* and was first introduced by the US Army in 1940. Nowadays, besides detection and location purposes, modern radar can identify, classify, track and image targets while suppressing undesirable echoes from the environment, also named clutter [1]. A simple radar, one that only measures range, can be explained as follows: when a pulse is transmitted

the radar clock is triggered to begin counting. The radio pulse travels at the speed of light until it is scattered from a target and goes back to the radar. The distance to the target is calculated by the time delay times the velocity of the light divided by two [2, 27, 9].

There are many applications in different fields where radars are indispensable, and not necessarily the army. For instance, in applications such as weather forecasting, navigation, collision avoidance, academic research, etc. Table 2.1 exhibits some applications for radars in different scenarios.

Table 2.1 – Applications of radar [27].

Civil:	
Ground-based	Air traffic control Sea traffic control Weather forecasting Speed traps Intruder alarms Radar astronomy Ground probing Industrial measurement
Sea-borne	Navigation Collision avoidance
Air-borne	Altimeters Navigation Weather
Space-borne	Studying Earth resources Sea sensing Manipulating spacecraft Mapping planets and minor bodies
Military:	
Detection	of own forces or enemy forces
Tracking	of air, sea, land, or space targets
Guidance	of own weapons systems

Since all radars use radio-frequency waves, there is a specific part of the radio-electric spectrum for these systems. Normally radars operate over the range of 3 MHz to 300 GHz. Along this wide range exist dedicated frequency ranges for radar systems

authorized by the International Telecommunications Union (ITU) [1, 27, 9]. Table 2.2 shows the range frequency of each band.

Table 2.2 – Frequencies for radar systems [1].

Band	**ITU Radar Frequency**
VHF (30–300 MHz)	138–144 MHz
UHF (0.3–1 GHz)	420–450 MHz
	890–942 MHz
L (1–2 GHz)	1.215–1.400 GHz
S (2–4 GHz)	2.3–2.5 GHz
	2.7–3.7 GHz
C (4–8 GHz)	5.250–5.925 GHz
X (8–12 GHz)	8.5–10.68 GHz
Ku ("under" K-band) (12–18 GHz)	13.4–14.0 GHz
	15.7–17.7 GHz
K (18–27 GHz)	24.05–24.25 GHz
	24.65–24.75 GHz
Ka ("above" K-band) (27–40 GHz)	33.4–36.0 GHz
V (40–75) GHz	59.0–64.0 GHz
W (75–110) GHz	76.0–81.0 GHz
	92.0–100.0 GHz
mm (100–300 GHz)	126.0–142.0 GHz
	144.0–149.0 GHz
	231.0–235.0 GHz
	238.0–248.0 GHz

2.2.2 Radar Cross Section

The Radar Cross Section (RCS), also named the echo area, is a measure of the reflective strength of a target usually represented by the letter σ [28]. Depending on the target's geometrical form two approaches can be taken to describe the σ parameter. Firstly, for simple geometrical bodies (e.g., regular polygons), the σ value can be easily obtained by deterministic expressions that already exist in the literature. On the other hand, when complex geometrical bodies are studied (e.g., aircraft), a stochastic approach must be taken [9]. This chapter focuses on the second approach.

2.2.2.1 Fluctuating targets

When a complex geometrical body changes the aspect angle due to its motion is named fluctuating target. As it was mentioned, these cases are better described by a PDF. A typical classification of fluctuating targets is done by Swerling models. The Swerling models are a set of PDFs where each PDF describes a certain fluctuating target type. Swerling models can be divided into two branches according to the fluctuations rate type. The first one is scan to scan fluctuation rate and the second is pulse to pulse

fluctuation rate. Generally, the slowly fluctuating targets are described as scan-to-scan fluctuation rate types. Also in modern radar systems, the term scan-to-scan is usually replaced by dwell to dwell fluctuation rate. The main two PDFs of the Swerling models are the Rayleigh and the fourth degree Chi-Squared distribution [1]. Table 2.3 summarizes the aforementioned.

Table 2.3 – Swerling models.

Case:	**Distribution:**	**Fluctuation Rate:**
Swerling I	Rayleigh	Scan to scan
Swerling II	Rayleigh	Pulse to pulse
Swerling III	Chi-Squared, degree 4	Scan to scan
Swerling IV	Chi-Squared, degree 4	Pulse to pulse

As mentioned earlier, some types of clutter (e.g. sea and ground clutter) are not well described by Swerling models. For instance, field measurements have proved that these types of clutter are better fit by long-tail distributions (e.g. Weibull distribution). Figure 2.1 and Figure 2.2 illustrate how Weibull and Rayleigh distributions shapes differ. The red and blue vertical dashed lines represent the threshold, a key parameter in the detection process, calculated for each distribution. As noted, for the same value of PFA (area under the curve after the threshold) the computed threshold is not the same (see Figure 2.2) and a lower threshold could result in unwanted false alarms; hence, it is essential to work with a distribution that better describes the clutter. [1, 29].

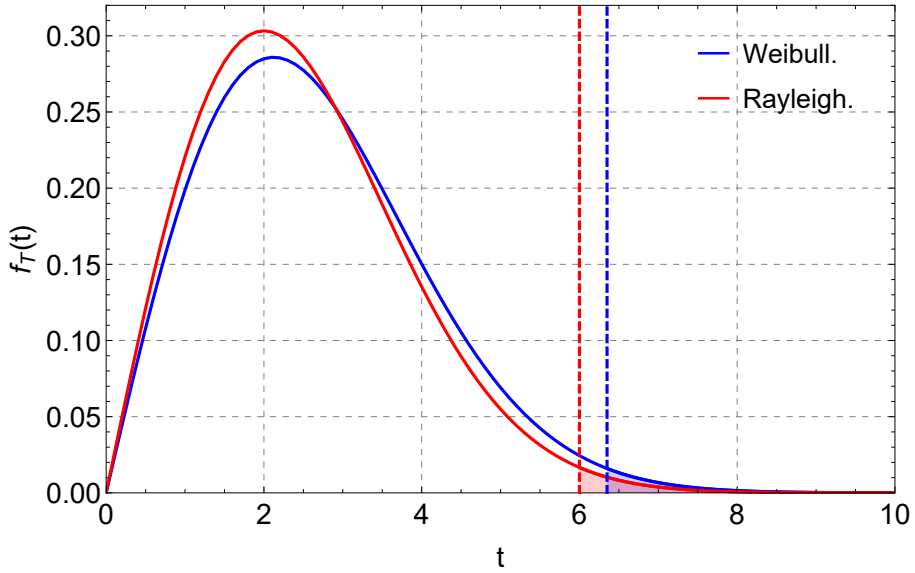

Figure 2.1 – Weibull distribution *vs* Rayleigh distribution.

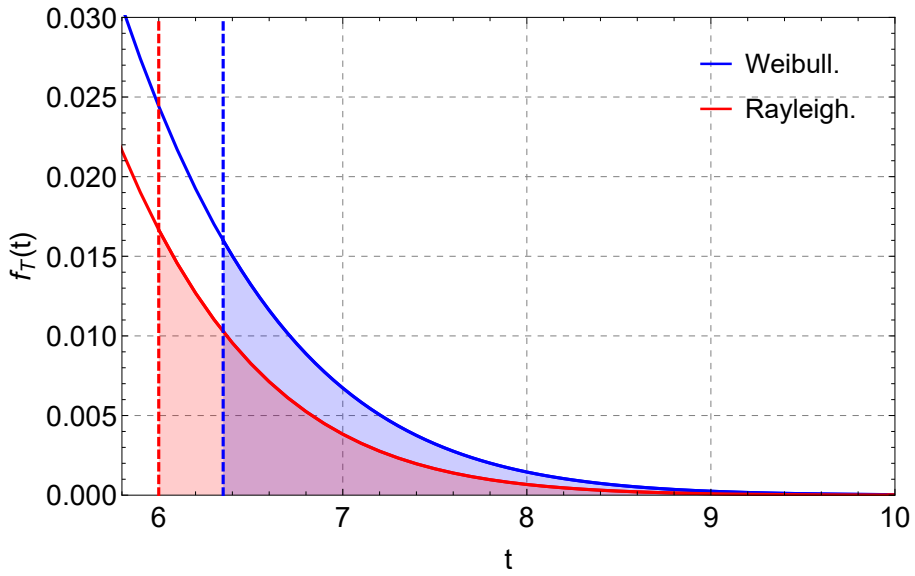

Figure 2.2 – Difference between threshold values for Weibull and Rayleigh distributions.

2.2.3 Radar Detection

A received radar echo signal is composed of clutter return and may, or may not contain a target echo signal. Since clutter and target signals are modeled as random processes the decision concerning the presence or absence target is statistical in nature. In problems where we need to infer something based on random phenomena we make use of the statistical decision theory [2]. The main elements of a statistical decision problem are:

- A set of hypothesis that describe all possible events.
- Data related to the established hypothesis from which we want to infer the true phenomena.
- A decision rule that evaluates the data to determine which hypothesis fulfilled.
- A criterion of optimally that reflects the cost of correct and incorrect decisions.

In Radar systems, the detection process can be explained with the aid of Figure 2.3. In the first stage, the signal that reaches a radar is filtered at its intermediate frequency. Then, the signal passes through a linear or square envelope detector. Next, the output of the envelope detector is compared with a predetermined threshold. Finally, the decision is made based one of two possible outcomes: presence or absence of a target. If the envelope detector's output surpasses the known threshold the presence of a target is declared, otherwise, the signal is assumed to contain clutter returns only [1, 9].

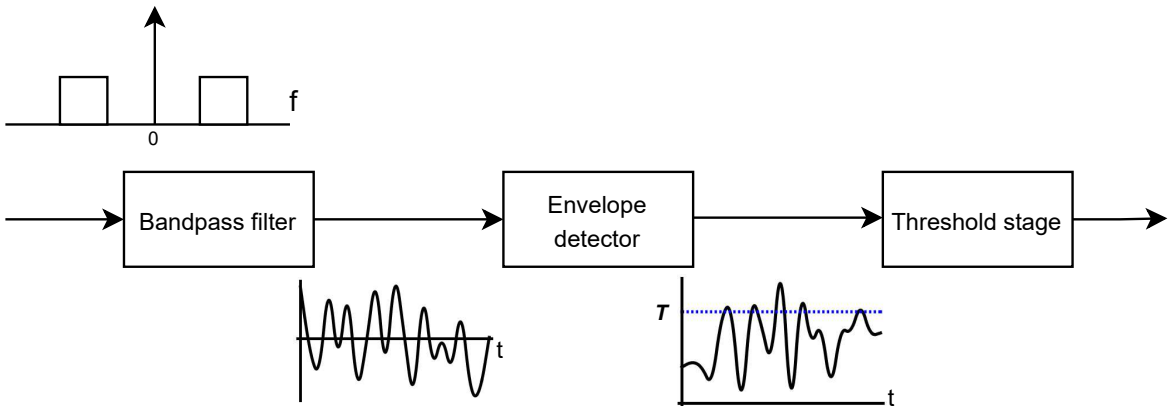

Figure 2.3 – Basic Radar Detector.

Given the importance of the threshold's value in the detection process, there are many approaches to determine it. Among the most important we have: Neyman-Person (NP) criterion and the CFAR technique [1]. The NP method fixes a PFA and then maximizes the PD for a given signal-to-noise ratio (SNR). The downside of this approach is that the threshold is set without considering any clutter variation leading to high false alarm rates [30]. To counteract this while considering a more realistic scenario where the clutter is fluctuating, the CFAR technique arises.

2.2.3.1 CFAR technique

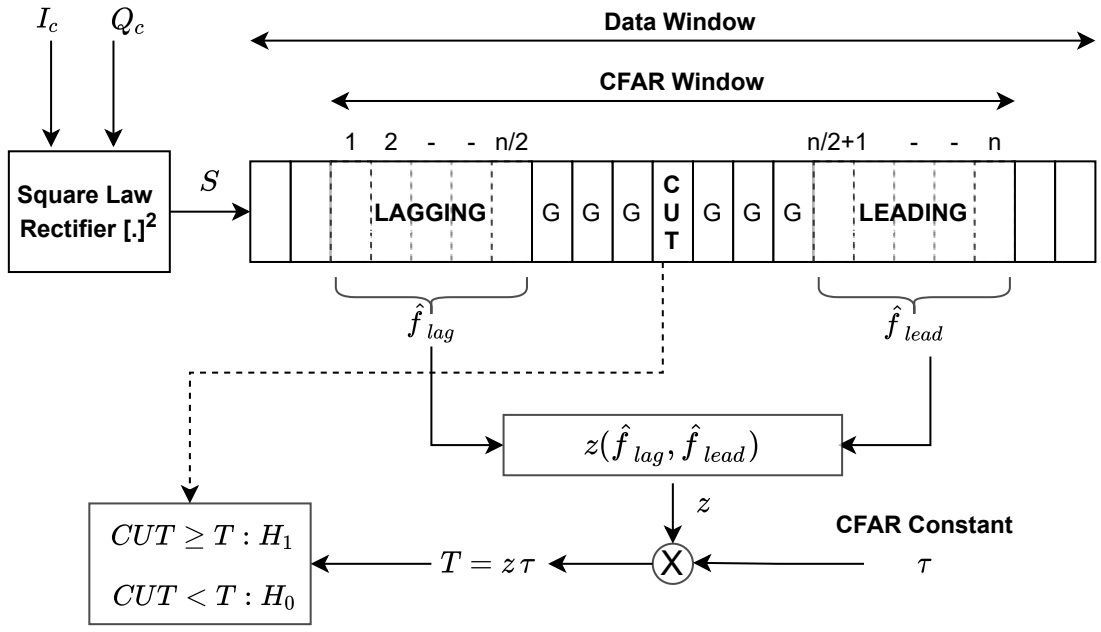

Figure 2.4 – General CFAR scheme.

A general CFAR scheme is shown in Fig 2.4. The baseband signals I_c and Q_c after the square law rectifier are represented by a single signal S. The S signal is then stored as a vector of size M, known as the data window. The CFAR window is composed of a subset of data window samples that are distributed between the lagging and leading windows, the guard cells, and the cell under test (CUT). The samples in the lagging and leading windows enter in a function z to obtain a statistic about the samples. In the case of the CA-CFAR detector, the function z calculates the average between leading and lagging samples. The z value times the CFAR constant τ is then compared with the CUT to make a decision for the presence or absence of a target. Notice that the CA-CFAR detector is not an optimum detector, but is widely used due to its low complexity [1].

2.2.4 Sum of Random Variables

Since the sum of random variables (RVs) is indispensable in the CFAR technique, a brief overview of this topic is presented below.

The probability theory establishes that the sum of a number of real RVs is another real RV. Assuming that the RVs are i.i.d. the sum PDF can be obtained by convoluting their PDFs [31, 32]. To exemplify, let Z denote the sum of N RVs, X_i.

$$Z = \sum_{i=1}^{N} X_i. \tag{2.1}$$

For $N = 2$ we have

$$f_Z(z) = \int_0^z p(x) \times p(z - x)\, \mathrm{d}x. \tag{2.2}$$

Now, extending the definition for N RVs we have

$$f_Z(z) = p(x_1) * p(x_2) * p(x_3) * ..... * p(x_N). \tag{2.3}$$

When following the convolution approach is quite difficult to obtain general expressions for the sum of N RVs. For this, an approach based on the characteristic functions of RVs is more useful [31, 32]. The characteristic function of a RV that follows a certain distribution $p(x)$ is defined as

$$C_X(\omega) = \int_{-\infty}^{\infty} \exp^{(j\omega x)} p(x)\, \mathrm{d}x. \tag{2.4}$$

Since the characteristic function is related to the Fourier transform, the sum of N random variables can be obtained as

$$C_Z(\omega) = \prod_{i=1}^{N} C_X(\omega), \tag{2.5}$$

where for i.i.d. RVs, (2.5) is reduced to

$$C_Z(\omega) = [C_X(\omega)]^N. \tag{2.6}$$

The inverse function $f_Z(z)$ can then be obtained with the inverse Fourier transform

$$f_Z(z) = \frac{1}{2\pi} \int_{-\infty}^{\infty} C_Z(\omega) \exp^{(-j\omega z)} \, \mathrm{d}\omega. \tag{2.7}$$

2.2.4.1 Sum of N i.i.d. Weibull RVs

Formulations for the PDF and CDF of the sum of N i.i.d Weibull RVs were recently introduced in [25]. To do so, the authors derived and used the following characteristic function of the Weibull distribution

$$C_Z(s) = k \left(\frac{1}{s\lambda}\right)^k \sum_{i=0}^{\infty} \frac{s^{-ki}\Gamma(ik+k)\left(-\left(\frac{1}{\lambda}\right)^k\right)^i}{i!}. \tag{2.8}$$

Advanced mathematical techniques such as *residues theorem* and *formal power series* were employed to derive the PDF and CDF that are respectively given by

$$f_Z(z) = z^{-1} k^N \left(\frac{z}{\lambda}\right)^{kN} \sum_{i=0}^{\infty} \frac{z^{ik}\delta_i}{\Gamma(ik+kN)} \tag{2.9}$$

$$F_Z(z) = k^N \left(\frac{z}{\lambda}\right)^{kN} \sum_{i=0}^{\infty} \frac{z^{ik}\delta_i}{\Gamma(ik+kN+1)}, \tag{2.10}$$

where k and λ are the shape and scale parameters of the Weibull distribution, N is the number of RVs and δ_i are recursive coefficients given by

$$\delta_0 = \Gamma(k)^N \tag{2.11}$$

$$\delta_i = \frac{1}{i\Gamma(k)} \sum_{l=1}^{i} \frac{\delta_{i-l}(-i+lN+l)\Gamma(lk+k)\left(-\left(\frac{1}{\lambda}\right)^k\right)^l}{l!}. \tag{2.12}$$

Expressions (2.9) and (2.10) were validated via MC simulations as shown in Figure 2.5 and Figure 2.6. Figures were taken from [25].

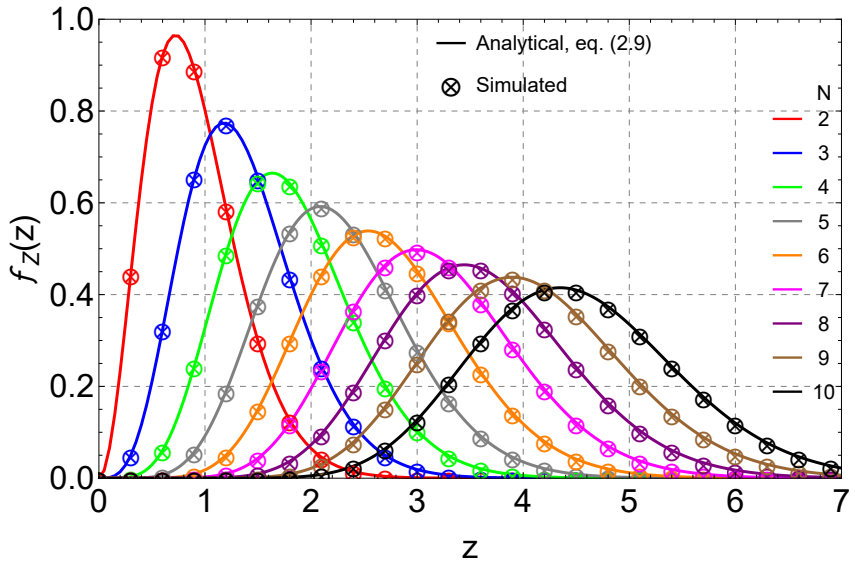

Figure 2.5 – PDF of the sum of Weibull variates considering $k = 1.5$, $\lambda = 0.5$, and different values of N.

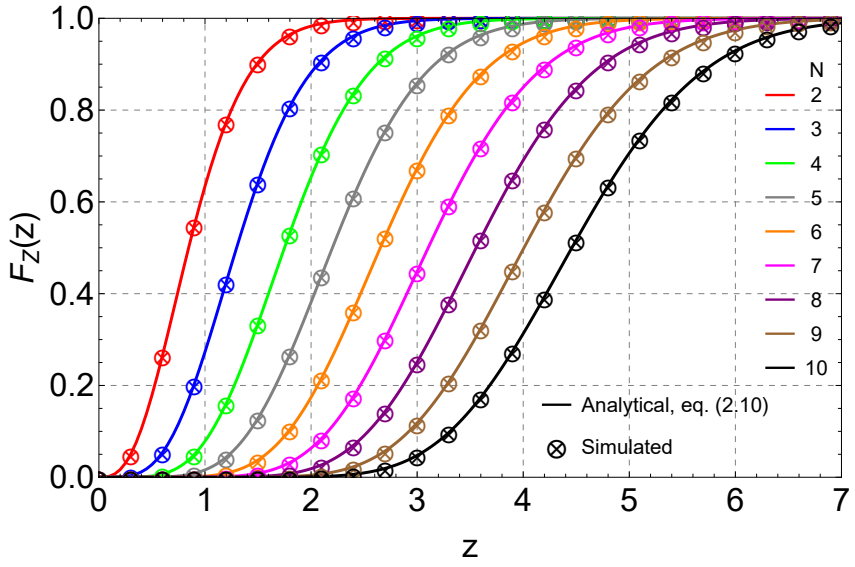

Figure 2.6 – CDF of the sum of Weibull variates considering $k = 1.5$, $\lambda = 0.5$, and different values of N.

2.3 Main Contributions

In this section, we introduce the main contributions of this chapter. First, we analyze the sum of N i.i.d Weibull variates. Then, we characterize the CUT's statistics, and finally, we present the derivation of the novel formulations for PD and PFA.

2.3.1 Analysing the sum of N i.i.d Weibull variates

Since (2.9) is the basis of this work, further analysis of the expression is done. As we note (2.9) is in terms of an infinite sum that cannot be expressed in closed form. In computationally terms it is not possible to execute the infinite sum, thus the expression must be bounded. When an upper limit of summation is set, the function diverges to infinity at a given value of z as illustrated in Figure 2.7. As depicted, for upper limit values of 100, 200, and 300, the function diverges at z =10, 13.5, and 16.2, respectively. To counteract the expression's divergence effects when computing the PFA and PD for a CA-CFAR detector, definite integrals with interval $[0, b]$ are used; where b denotes the bound before the equation begins to diverge. More details of this analysis are presented in subsection 2.3.3.

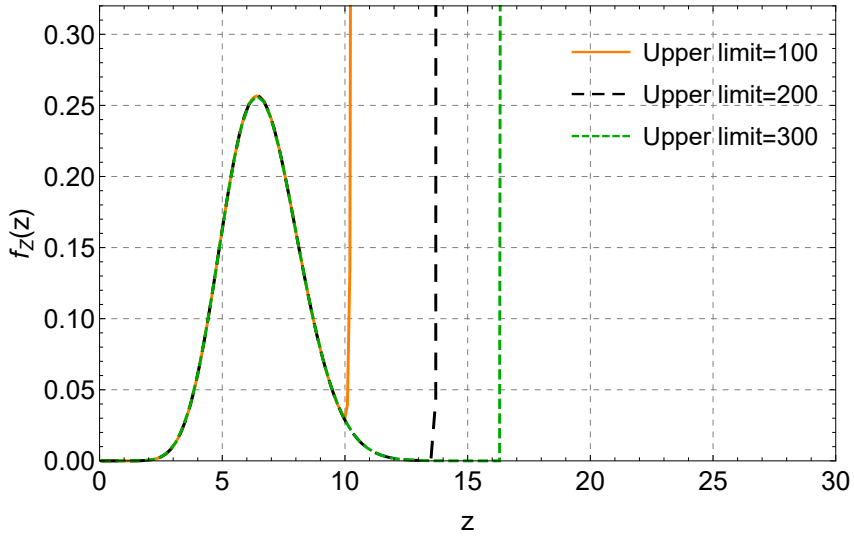

Figure 2.7 – Eq. (2.9) considering $k = 2$, $\lambda = 1.5$, $N = 5$ and different values of upper limit.

2.3.2 System Model

In this subsection, we introduce the system model and characterize the CUT and CFAR window statistic..

For the analysis, we consider an homogeneous Weibull-distributed clutter A and an exponentially distributed target B with PDFs given, respectively, by

$$f_A(a) = \frac{k}{\lambda}\left(\frac{a}{\lambda}\right)^{k-1} \exp\left[-\left(\frac{a}{\lambda}\right)^{k}\right] \qquad a \geq 0 \tag{2.13}$$

$$f_B(b) = \eta \exp\left[-\eta\, b\right], \qquad b \geq 0 \tag{2.14}$$

where $k > 0$ and $\lambda > 0$ are the shape and scale parameters of the Weibull distribution, respectively, and η is the rate parameter of the exponential distribution.

In order to analyze the performance of a CA-CFAR detector, we consider that the CUT is governed by the following binary hypothesis test [33, 34, 19]:

$$H_0(\text{clutter only}): \; T = A \tag{2.15}$$

$$H_1(\text{target-plus-clutter}): \; T = B + A, \tag{2.16}$$

where hypothesis H_0 denotes the presence of the clutter signal only, whereas hypothesis H_1 denotes the presence of both target and clutter signals.

2.3.2.1 CUT's Statistics

From (2.15), the PDF and CDF of T under hypothesis H_0 are given respectively by

$$f_T(t|H_0) = \frac{k}{\lambda}\left(\frac{t}{\lambda}\right)^{k-1} \exp\left[-\left(\frac{t}{\lambda}\right)^k\right], \qquad t \geq 0 \tag{2.17}$$

$$F_T(t|H_0) = 1 - \exp\left[-\left(\frac{t}{\lambda}\right)^k\right], \qquad t \geq 0. \tag{2.18}$$

The exact PDF and CDF of T given hypothesis H_1 are derived in the upcoming proposition.

Proposition. *The PDF and CDF of T under hypothesis H_1 are given, respectively, by*

$$f_T(t|H_1) = \eta \exp[-\eta t] \sum_{j=0}^{\infty} \frac{(\eta\lambda)^j}{j!}\, \gamma\left(\frac{j+k}{k}, \left(\frac{t}{\lambda}\right)^k\right) \tag{2.19}$$

$$\begin{aligned} F_T(t|H_1) = &\sum_{j=0}^{\infty} \frac{(\eta\lambda)^j}{j!} \left[-\exp[-\eta t]\, \gamma\left(\frac{j+k}{k}, \left(\frac{t}{\lambda}\right)^k\right)\right. \\ &\left. + \sum_{m=0}^{\infty} \frac{(-\eta\lambda)^m}{m!}\, \gamma\left(\frac{j+k+m}{k}, \left(\frac{t}{\lambda}\right)^k\right)\right]. \end{aligned} \tag{2.20}$$

Proof. The sum PDF for (2.16) can be obtained by convoluting the marginal PDF of A and B as follows [35]

$$f_T(t|H_1) \triangleq \int_0^t f_A(\nu)\, f_B(t-\nu)\, \mathrm{d}\nu. \tag{2.21}$$

Replacing (2.13) and (2.14) into (2.21) and followed by some algebraic steps with the aid of [26, eq. (4.2.1)], we obtain

$$f_T(t|H_1) = \frac{k\,\eta}{\lambda} \exp[-\eta t] \int_0^t \exp\left[-\left(\frac{\nu}{\lambda}\right)^k\right] \left(\frac{\nu}{\lambda}\right)^{k-1} \sum_{j=0}^{\infty} \frac{(\eta\,\nu)^j}{j!}\, \mathrm{d}\nu,$$

interchanging the order of integration by employing the Fubini's theorem[1] we have

$$f_T(t|H_1) = \frac{k\,\eta}{\lambda} \exp[-\eta t] \sum_{j=0}^{\infty} \frac{(\eta)^j}{j!} \int_0^t \exp\left[-\left(\frac{\nu}{\lambda}\right)^k\right] \left(\frac{\nu}{\lambda}\right)^{k-1} (\nu)^j\, \mathrm{d}\nu. \tag{2.22}$$

[1] Hereinafter, all interchanges in the order of integration will be carried guaranteeing that the Fubini's conditions are fulfilled.

Evaluating the resultant integral, we obtain (2.19). From (2.19), the CDF of T can be calculated as

$$\begin{aligned} F_T(t|H_1) &\triangleq \int_0^t f_T(\nu|H_1)\mathrm{d}\nu \\ &= \eta \int_0^t \exp\left[-\eta\nu\right] \sum_{j=0}^{\infty} \frac{(\eta\,\lambda)^j}{j!}\, \gamma\left(\frac{j+k}{k}, \left(\frac{\nu}{\lambda}\right)^k\right) \mathrm{d}\nu. \end{aligned} \tag{2.23}$$

Finally, interchanging the order of integration in (2.23) and then integrating the resulting expression by parts, we get (2.20), which completes the proof. Figs. 2.8 and 2.9 illustrate the analytical expressions (2.19) and (2.20) versus the Monte-Carlo simulation for different values of k, λ and η. The plots show the agreement between analytical and simulated hence validating the formulations. The expression (2.19) is also justified by different fit tests. Table 2.4 shows the aforementioned. As depicted, all the $P-values$ for the different types of tests are greater than 0.9 demonstrating by this metric the huge agreement between the simulated and analytical expression. For more details about the tests see [36].

Table 2.4 – Distribution fit tests

Goodness of fit test:	**Statistic:**	**P-value:**
Anderson-Darling	0.272319	0.95739
Cramér-von Mises	0.0353659	0.955405
Kolmogorov-Smirnov	0.0126	0.953986
Kuiper	0.0218	0.928793

■

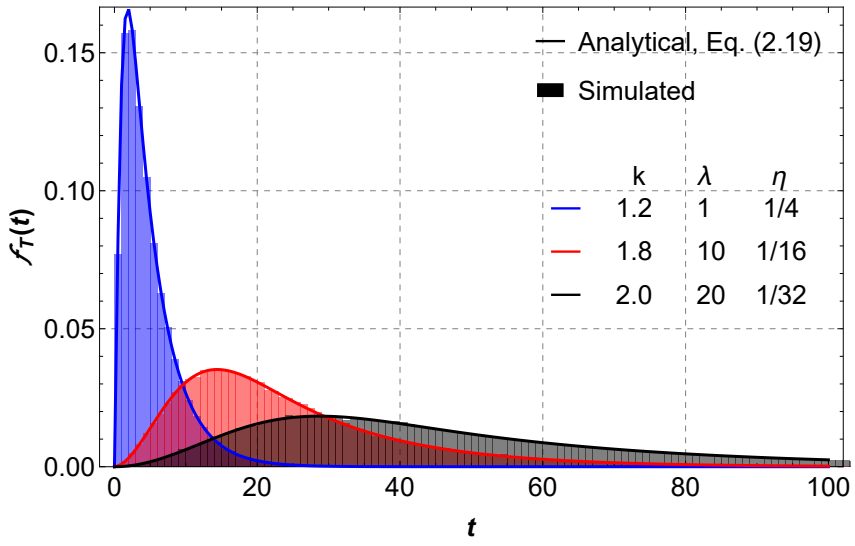

Figure 2.8 – PDF of $f(t|H_1)$ for different values of k, λ, η and 100 as the upper limit of the summation.

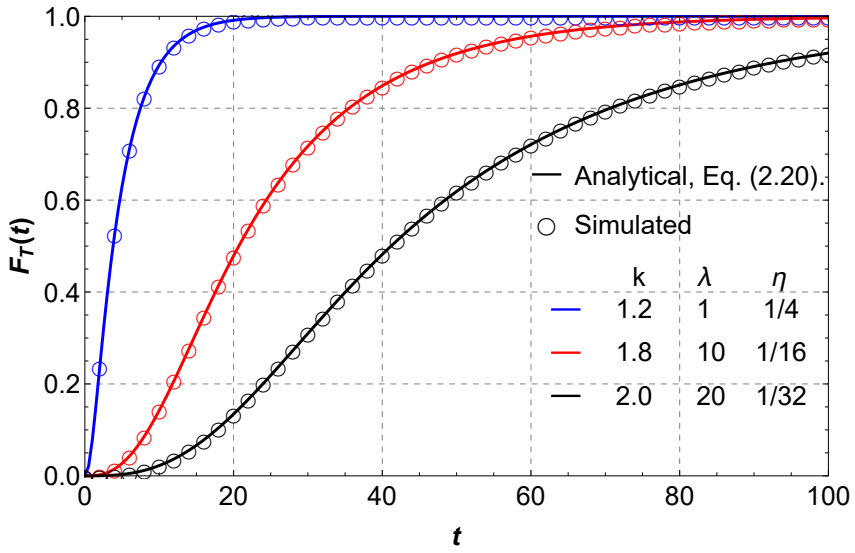

Figure 2.9 – CDF of $F(t|H_1)$ for different values of k, λ, η and 100 as the upper limit of the summation.

2.3.2.2 CFAR Window Statistics

In a CA-CFAR detector, the estimated interference power, Z, is computed by averaging N i.i.d. clutter samples within the CFAR window. Thus, leveraging on (2.9) and after a conventional transformation of variables, the PDF of Z can be written as

$$\tilde{f}_Z(z) = z^{-1} k^N \left(\frac{zN}{\lambda}\right)^{kN} \sum_{i=0}^{\infty} \frac{(zN)^{ik} \delta_i}{\Gamma(ik + kN)}, \tag{2.24}$$

where δ_i are the recursive coefficients that can be calculated from (2.11) and (2.12).

2.3.3 CA-CFAR Detection

In this section, we analyze the performance of a CA-CFAR detector working over homogeneous Weibull-distributed clutter environments.

2.3.3.1 Probability of False Alarm

The probability of deciding that the received signal contains only noise defined as the probability of false alarm [1]. Mathematically, the PFA of a CA-CFAR detector is found by integrating from 0 to infinity the conditioned PFA, $\overline{P_{\text{FA}}}$, over all possible values of the interference statistic $f_Z(z)$.

$$P_{\text{FA}} = \int_0^{\infty} \overline{P_{\text{FA}}}\, f_Z(z)\, \mathrm{d}z. \tag{2.25}$$

Because of the divergence of (2.9), the integral's interval is going to be limited to $[0, b]$. Therefore, we define $\widehat{P_{\text{FA}}}$ as high accurate approximation of (2.25) and is expressed as

$$\widehat{P_{\text{FA}}} = \int_0^b \overline{P_{\text{FA}}}\, f_Z(z)\, \mathrm{d}z, \tag{2.26}$$

where b represents the bound before (2.9) begins to diverge. To guarantee that no *"relevant information"* is lost when the bounded integral is calculated, the value of b must be found equating (2.9) to a very low value Φ (e.g. $\leq 10^{-4}$). Mathematically b is calculated as

$$b^{-1}k^N \left(\frac{b}{\lambda}\right)^{kN} \sum_{i=0}^{UL} \frac{(b)^{ik}\delta_i}{\Gamma(ik+kN)} = \Phi, \tag{2.27}$$

where UL denotes the upper limit of the sum (e.g. 200) therefore (2.27) can be easily solved by any math software.

The conditioned PFA, $\overline{P_{\text{FA}}}$, can be calculated from (2.18) as follows

$$\begin{aligned}\overline{P_{\text{FA}}} &\triangleq \int_{\frac{\tau z}{N}}^{\infty} f_T\left(t|H_0\right)\mathrm{d}t \\ &= 1 - F_T\left(\frac{\tau z}{N}|H_0\right) \\ &= \exp\left[-\left(\frac{\tau z}{\lambda N}\right)^k\right],\end{aligned} \tag{2.28}$$

where the lower bound of the integral, $\frac{\tau z}{N}$, represent the CA-CFAR constant times z (in order to get a result as function of the interference $f_Z(z)$) and divided by the number of samples N. The division by N in the bound is done because we are using the original expression, (2.9), that is not yet normalized by the number of samples. When the normalized sum is used, in this case (2.24), we do not need the division by N in the bound.

To illustrate the impact of not considering the divergence effect of (2.9), we derive both expressions (2.25) and (2.26). Thus, replacing (2.9) and (2.28) into (2.25) and (2.26), followed by a change in the order of integration along with several mathematical manipulations, we obtain

$$P_{\text{FA}} = k^{-1+N}\left(\frac{N}{\tau}\right)^{kN} \sum_{i=0}^{\infty}\left(\frac{\lambda N}{\tau}\right)^{ik} \frac{\Gamma(i+N)}{\Gamma(ik+Nk)}\delta_i, \tag{2.29}$$

$$\widehat{P_{\text{FA}}} = k^{-1+N}\left(\frac{N}{\tau}\right)^{kN} \sum_{i=0}^{UL}\left(\frac{\lambda N}{\tau}\right)^{ik} \frac{\gamma\left(i+N, \left(\frac{b\,\tau}{\lambda N}\right)^k\right)}{\Gamma(ik+Nk)}\delta_i. \tag{2.30}$$

Note that when b and UL tend to infinity, (2.30) reduces to (2.29). Figure 2.10 illustrates the resultant PFA for different values of threshold τ where both (2.29) and (2.30) were computed with $UL = 500$. As depicted, for $\tau \leq 4.9$ expression (2.29) diverges

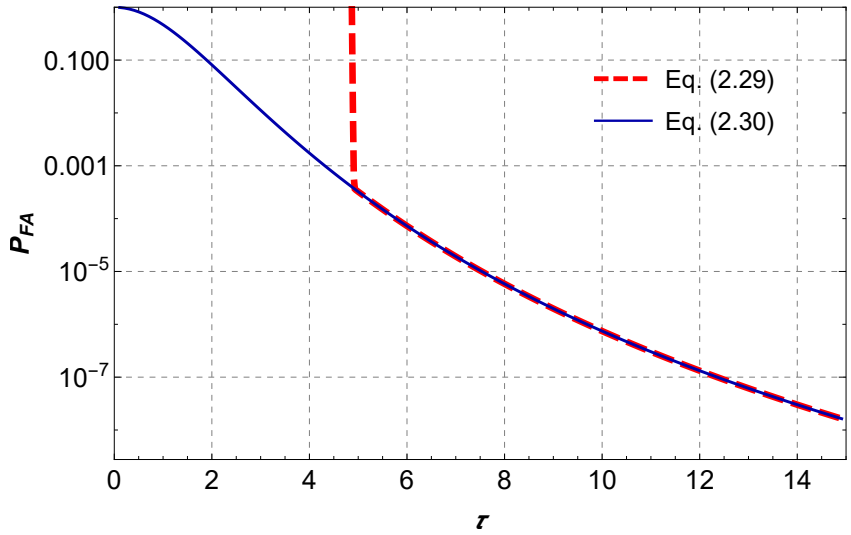

Figure 2.11 – Replica of Figure 2.10 in log scale.

and the PFA value is infinite while expression (2.30) does indeed outputs PFA values that are between 0 and 1 for any τ. Furthermore, Figure 2.11 shows, in log scale, how the PFA values match between the two expressions for threshold values greater than 4.9.

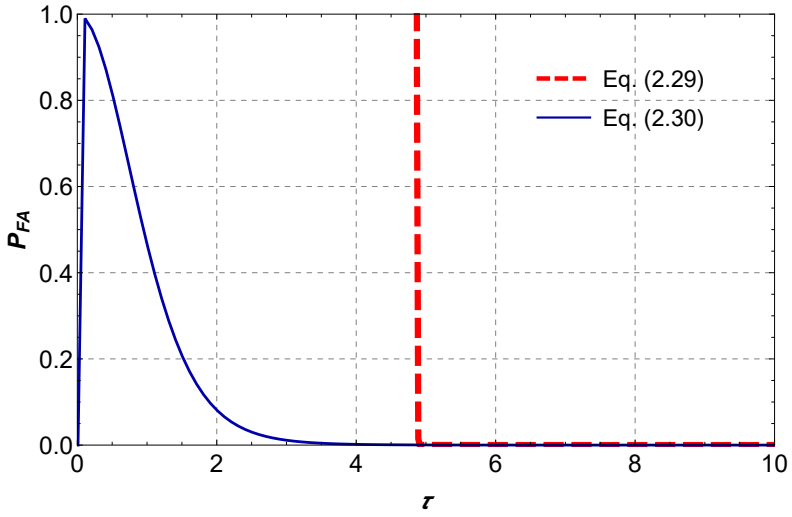

Figure 2.10 – Eq. (2.29) and eq.(2.30) for $k = 2$, $\lambda = 1.5$, $N = 5$, $b = 13.5$ and different values of threshold τ.

Moreover, it is possible to show that (2.29) and (2.30) are independent of the clutter power, λ^k, and can be rewritten respectively as

$$P_{\text{FA}} = k^{-1+N} \left(\frac{N}{\tau}\right)^{kN} \sum_{i=0}^{\infty} \left(\frac{N}{\tau}\right)^{ik} \frac{\Gamma(i+N)}{\Gamma(ik+Nk)} \psi_i, \tag{2.31}$$

$$\widehat{P_{\text{FA}}} = k^{-1+N} \left(\frac{N}{\tau}\right)^{kN} \sum_{i=0}^{UL} \left(\frac{N}{\tau}\right)^{ik} \frac{\gamma\left(i+N, \left(\frac{b\tau}{N}\right)^k\right)}{\Gamma(ik+Nk)} \psi_i \tag{2.32}$$

where the coefficients ψ_i can be obtained recursively by

$$\psi_0 = \Gamma(k)^N \tag{2.33}$$

$$\psi_i = \frac{1}{i\Gamma(k)} \sum_{l=1}^{i} \frac{\psi_{i-l}(-i+lN+l)\Gamma(lk+k)\,(-1)^l}{l!}. \tag{2.34}$$

Appendix A proves the aforementioned for (2.29). Following a similar procedure, it can be also demonstrated for (2.30). Furthermore, Appendix B shows that (2.31) absolutely converge $\forall k \geq 1$.

2.3.3.2 Probability of detection

The probability of detection seems the likelihood of detecting a target in a received signal. Following a similar approach as in Section 2.3.3.1, the PD of a CA-CFAR detector can be obtained with either

$$P_{\mathrm{D}} = \int_0^{\infty} \overline{P_{\mathrm{D}}}\, f_Z(z)\, \mathrm{d}z, \tag{2.35}$$

or

$$\widehat{P_{\mathrm{D}}} = \int_0^{b} \overline{P_{\mathrm{D}}}\, f_Z(z)\, \mathrm{d}z, \tag{2.36}$$

in which $\overline{P_{\mathrm{D}}}$ corresponds to the conditioned PD.

From (2.19) and after some algebraic manipulations, the conditioned PD can be calculated as

$$\begin{aligned}
\overline{P_{\mathrm{D}}} \triangleq & \int_{\frac{\tau z}{N}}^{\infty} f_T\left(t|H_1\right) \mathrm{d}t \\
=& 1 - F_T\left(\frac{\tau z}{N}|H_1\right) \\
=& \sum_{j=0}^{\infty} \frac{(\eta\lambda)^j}{j!} \left[\exp\left[-\frac{\eta\,\tau\,z}{N}\right] \gamma\left(\frac{j+k}{k}, \left(\frac{\tau\,z}{\lambda N}\right)^k\right)\right. \\
&\left. + \sum_{m=0}^{\infty} \frac{(-\eta\lambda)^m}{m!}\, \Gamma\left(\frac{j+k+m}{k}, \left(\frac{\tau\,z}{\lambda N}\right)^k\right)\right].
\end{aligned} \tag{2.37}$$

Finally, substituting (2.37) and (2.9) into (2.35) and (2.36), and followed by a change in the order of integration along with lengthy algebraic manipulations with the aid of [26, eq. (6.5.3)] and [26, eq. (4.2.1)], we obtain

$$\begin{aligned}
P_{\mathrm{D}} =& k^N \left(\frac{N}{\lambda\tau}\right)^{kN} \sum_{j=0}^{\infty}\sum_{i=0}^{\infty} \frac{(\eta\lambda)^j}{j!} \Gamma\left(\frac{j+k}{k}\right) \left(\frac{N}{\tau}\right)^{k\,i} \delta_i \\
&\times \left[\eta^{-k(i+N)} - \frac{(\lambda)^{k(i+N)}}{\Gamma(k(i+N)+1)} \sum_{m=0}^{\infty} \frac{(-\eta\lambda)^m \Gamma\left(\frac{j+m+k(i+N+1)}{k}\right)}{m!\,((k(i+N)+m)}\right],
\end{aligned} \tag{2.38}$$

and

$$\begin{aligned}\widehat{P_{\mathrm{D}}} =& k^N \left(\frac{1}{\lambda}\right)^{kN} \sum_{j=0}^{UL} \frac{(\eta\lambda)^j}{j!} \sum_{i=0}^{UL} \left(\frac{\tau}{N}\right)^{-k(i+N)} \frac{\delta_i}{\Gamma(ik+Nk)} \\ &\times \left\{ \Gamma\left(\frac{j+k}{k}\right) \eta^{-k(i+N)} \gamma\left(k(i+N), \frac{b\,\eta\,\tau}{N}\right) \right. \\ &- \sum_{m=0}^{UL} \frac{(-\eta\,\lambda)^m}{m!} \left[\frac{1}{k(i+N)+m} \left[\gamma\left(\frac{k(i+N+1)+j+m}{k}, \left(\frac{b\,\tau}{\lambda N}\right)^k \right) \right.\right. \\ &+ \left.\left(\frac{b\,\tau}{\lambda\,N}\right)^{k\left(i+\frac{m}{k}+N\right)} \Gamma\left(\frac{j+k}{k}, \left(\frac{b\,\tau}{N\,\lambda}\right)^k\right) \right] \\ &- \frac{1}{k(i+N)} \left[\gamma\left(\frac{k(i+N+1)+j+m}{k}, \left(\frac{b\,\tau}{\lambda N}\right)^k \right) \right. \\ &\left.\left.\left. + \left(\frac{b\,\tau}{\lambda\,N}\right)^{k(i+N)} \Gamma\left(\frac{j+k+m}{k}, \left(\frac{b\,\tau}{N\,\lambda}\right)^k\right) \right] \right] \right\}. \end{aligned} \tag{2.39}$$

Following a similar procedure as in Appendix B, it can be shown that (2.38) also converges absolutely $\forall k \geq 1$. Eqs. (2.31), (2.32), (2.38) and (2.39) are the main contributions of this chapter.

2.3.4 Numerical Results

In this section, we validate our derived expressions via Monte-Carlo simulations. The receiver operating characteristic (ROC) curves are presented considering different parameter settings. The number of Monte-Carlo trials was set to 10^7.

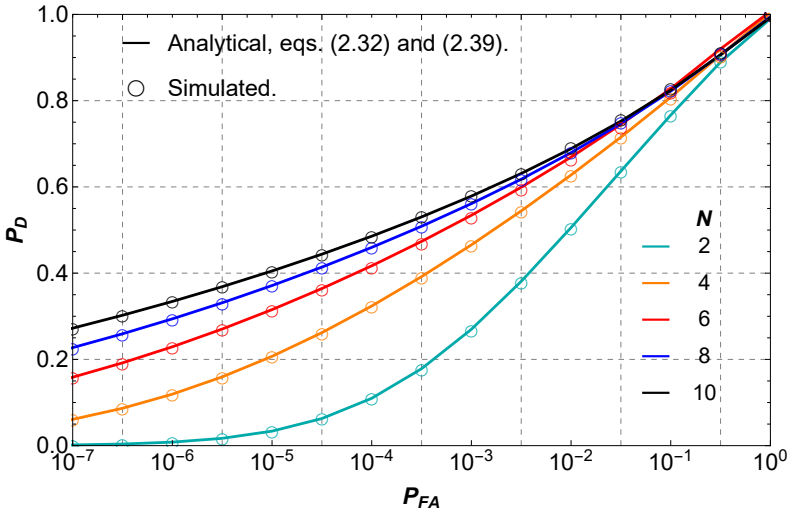

Figure 2.12 – ROC curves for $k = 1.5$, $\lambda = 1$, $\eta = 0.25$, and different values of N.

Figure 2.12 illustrates PD versus PFA considering different values of N. Notice how the PD improves as N grows, as expected. For instance, for a fixed $P_{\mathrm{FA}} = 10^{-4}$ and

$N = 2, 4, 6, 8, 10$, we obtain $P_{\mathrm{D}} = 0.1, 0.3, 0.41, 0.45, 0.48$, respectively.

Figure 2.13. illustrates PD versus PFA for different values of k. Notice how radar detection increases as k increases as well, evidencing the relevance of this parameter in radar performance analysis. For example, for $P_{\mathrm{FA}} = 10^{-5}$ and $k = 1, 1.4, 1.8, 2.0, 2.2$, we get $P_{\mathrm{D}} = 0.07, 0.33, 0.54, 0.61, 0.66$, respectively. To give a better understanding it is important to mention that shape values, k, between 1.4 and 1.8 are usually used to model the sea clutter [15]. Therefore, the exhibited results suggest the use of real k parameters according to the type of clutter.

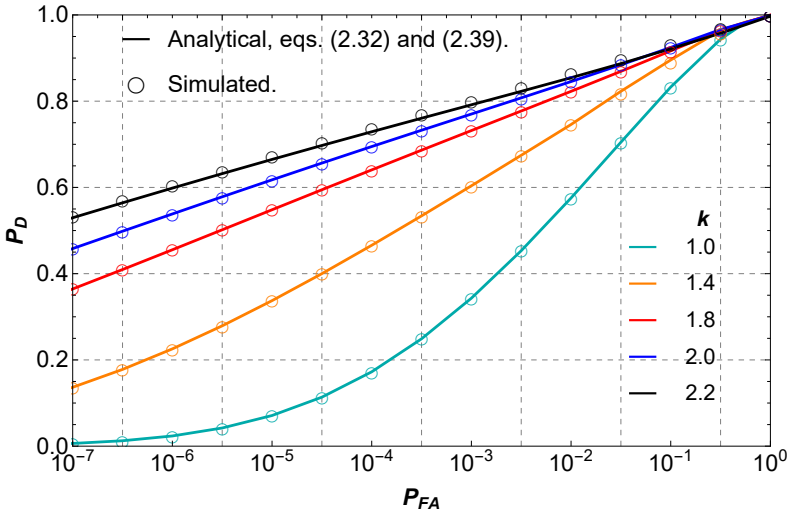

Figure 2.13 – ROC curves for $N = 6$, λ=1, $\eta = 0.1$, and different values of k.

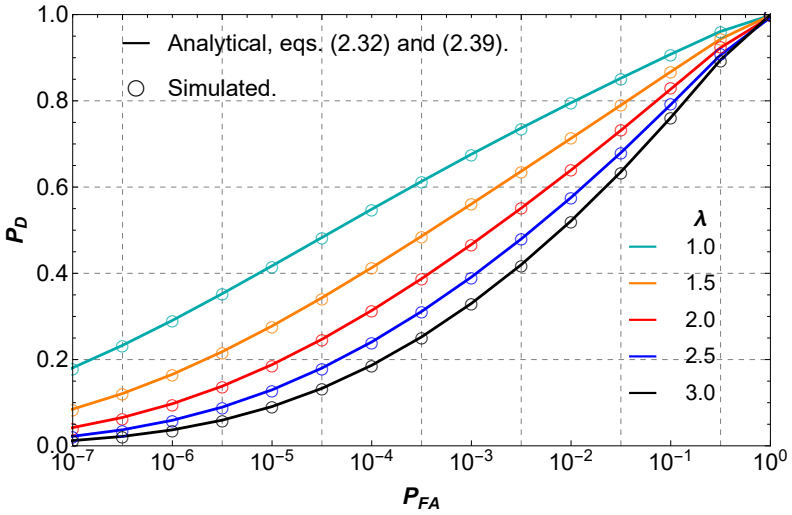

Figure 2.14 – ROC curves for $N = 4$, $k = 1.8$, $\eta = 0.1$, and different values of λ.

Finally, Figure 2.14. shows ROC curves varying the scale parameter λ. The curves exhibit that as the scale parameter increases the P_{D} decreases as expected since λ is directly related to the clutter power. For instance, we note that for $P_{\mathrm{FA}} = 10^{-3}$ and λ=1, 1.5, 2, 2.5, 3, the values of P_{D} are 0.67, 0.56, 0.46, 0.39 and 0.33 respectively. In

other words, all figures denote perfect agreement between our analytical expressions and numerical simulations, thus validating our results.

2.4 Conclusion

In this chapter, we provided generalized expressions for the PD and PFA of a CA-CFAR detector working over homogeneous Weibull-distributed clutter. These expressions allow for arbitrary values for the shape parameter of the Weibull distribution. Moreover, they are tractable and can be easily implemented in any mathematical software, thus serving as useful analytical tools for radar designers and engineers. Radar performance was quantified in terms of the PD versus PFA. All our expressions were validated via Monte-Carlo simulations.

2.5 Bibliography

[1] M. A. Richards, J. Scheer, W. A. Holm, and W. L. Melvin, *Principles of Modern Radar: Basic Principles*, 1st ed. West Perth, WA, Australia: SciTech, 2010.

[2] J. V. DiFranco and W. Rubin, *Radar detection*. Scitech, 2004.

[3] F. D. A. García, H. R. C. Mora, G. Fraidenraich, and J. C. S. Santos Filho, "Alternative representations for the probability of detection of non-fluctuating targets," *Electron. Lett.*, vol. 56, no. 21, pp. 1136–1139, Oct. 2020.

[4] M. I. Skolnik, *Introduction to Radar Systems*, 3rd ed. New York: McGraw-Hill, 2001.

[5] H. A. Meziani and F. Soltani, "Performance analysis of some CFAR detectors in homogeneous and non-homogeneous Pearson-Distributed clutter," *Signal Process.*, vol. 86, no. 8, p. 2115–2122, Aug 2006.

[6] M. Weiss, "Analysis of some modified Cell-Averaging CFAR processors in multiple-target situations," *IEEE Trans. Aerosp. Electron. Syst.*, vol. AES-18, no. 1, pp. 102–114, Jan 1982.

[7] Y.-r. Zhang, M.-g. Gao, and Y.-j. Li, "Performance analysis of typical mean-level CFAR detectors in the interfering target background," in *9th IEEE Conf. on Ind. Electron. and Appl.*, Oct 2014, pp. 1045–1048.

[8] A. Zaimbashi, M. Taban, and M. Nayebi, "Order Statistic and Maximum Likelihood distributed CFAR detectors in Weibull background," in *2007 IEEE Radar Conf.*, Jun 2007, pp. 491–496.

[9] N. Levanon, *Radar principles*, 1st ed. New York, NY, USA: Wiley, May 1988.

[10] C. M. Wong, C. H. Chang, W. Liu, and J. Fu, "CA-CFAR in Weibull background," in *2nd Int. Conf. on Microw. and Millimeter Wave Technol. Proc.*, 2000, pp. 691–694.

[11] A. Bentoumi, A. Mezache, and T. H. Kerbaâ, "Performance of non-parametric CFAR detectors in log-normal and k radar clutter," in *2018 Int. Conf. on Elect. Sciences and Technol. in Maghreb (CISTEM)*, Oct. 2018, pp. 1–4.

[12] Y. I. Abramovich and O. Besson, "Fluctuating target detection in fluctuating K-distributed clutter," *IEEE Signal Process. Lett.*, vol. 22, no. 10, pp. 1791–1795, May. 2015.

[13] R. R. Boothe, "The Weibull distribution applied to the ground clutter backscatter coefficient," Army missile command redstone arsenal al research and engineering, Tech. Rep., 1969.

[14] T. Bucciarelli, "CFAR problems in Weibull clutter," *Electron. Lett.*, vol. 21, no. 8, pp. 286–304, Apr. 1985.

[15] D. C. Schleher, "Radar detection in Weibull clutter," *IEEE Trans. Aerosp. Electron. Syst.*, vol. AES-12, no. 6, pp. 736–743, Nov. 1976.

[16] G. D. M. Vela, J. A. B. Portas, and J. R. C. Corredera, "Probability of false alarm of CA-CFAR detector in Weibull clutter," *Electron. Lett.*, vol. 34, no. 8, pp. 806–807, Apr. 1998.

[17] M. Sekine, S. Ohtani, T. Musha, T. Irabu, E. Kiuchi, T. Hagisawa, and Y. Tomita, "Weibull-distributed ground clutter," *IEEE Trans. Aerosp. Electron. Syst.*, vol. AES-17, no. 4, pp. 596–598, Jul. 1981.

[18] K. Siddiq and M. Irshad, "Analysis of the cell averaging CFAR in Weibull background using a distribution approximation," in *2nd Int. Conf. on Comput., Control and Commun.*, 2009, pp. 1–5.

[19] A. Abbadi, H. Bouhedjeur, A. Bellabas, T. Menni, and F. Soltani, "Generalized closed-form expressions for CFAR detection in heterogeneous environment," *IEEE Geosci. Remote Sens. Lett.*, vol. 15, no. 7, pp. 1011–1015, Jul. 2018.

[20] F. D. A. García, A. C. F. Rodriguez, G. Fraidenraich, and J. C. S. Santos Filho, "CA-CFAR detection performance in homogeneous Weibull clutter," *IEEE Geosci. Remote Sens. Lett.*, vol. 16, no. 6, pp. 887–891, Jun. 2019.

[21] F. D. A. García, H. R. C. Mora, G. Fraidenraich, and J. C. S. Santos Filho, "Square-law detection of exponential targets in Weibull-distributed ground clutter," *IEEE Geosci. Remote Sens. Lett.*, early access, Jul. 22, 2020, doi: 10.1109/LGRS.2020.3009304.

[22] F. D. A. García, A. C. F. Rodriguez, and G. Fraidenraich, "Highly accurate closed-form approximation for the probability of detection of Weibull fluctuating targets in non-coherent detectors," *IEEE Trans. Aerosp. Electron. Syst.*, early access, Jul. 14, 2021, doi: 10.1109/TAES.2021.3096867.

[23] V. Anastassopoulos and G. A. Lampropoulos, "Optimal CFAR detection in weibull clutter," *IEEE Trans. Aerosp. Electron. Syst.*, vol. 31, no. 1, pp. 52–64, 1995.

[24] R. Raghavan, "Analysis of CA-CFAR processors for linear-law detection," *IEEE Trans. Aerosp. Electron. Syst.*, vol. 28, no. 3, pp. 661–665, Jul, 1992.

[25] F. D. A. García, F. R. A. Parente, G. Fraidenraich, and J. C. S. Santos Filho, "Light exact expressions for the sum of weibull random variables," *IEEE Wireless Commun. Lett.*, early access, Aug. 06, 2021, doi: 10.1109/LGRS.2020.3009304.

[26] M. Abramowitz and I. A. Stegun, *Handbook of Mathematical Functions with Formulas, Graphs, and Mathematical Tables*, 10th ed. Washington, DC: US Dept. of Commerce: National Bureau of Standards, 1972.

[27] S. Kingsley and S. Quegan, *Understanding Radar Systems*. UK: McGraw-Hill, 1992.

[28] J. F. (Ed.), *IEEE Standard Dictionary of Electrical and Electronic Terms*, 3rd ed. New York: IEEE Press, 1984.

[29] E. F. Knott, J. F. Schaeffer, and M. T. Tulley, *Radar Cross Section*, 2nd ed. Scitech Publishing, Jun. 2004.

[30] S. Kay, *Fundamentals of Statistical Signal Processing Vol. II: Detection Theory*. New Jersey: Prentice-Hall, 1998, vol. 2.

[31] R. D. Yates and D. J. Goodman, *Probability and Stochastic Processes*, 2nd ed. New Jersey: John Wiley and Sons, 2005.

[32] A. Leon-Garcia, *Probability Statistics and Random Processes for Electrical Engineering*, 3rd ed. New Jersey: Pearson, 2008.

[33] X. W. Meng, "Performance analysis of OS-CFAR with binary integration for Weibull background," *IEEE Trans. Aerosp. Electron. Syst.*, vol. 49, no. 2, pp. 1357–1366, Apr. 2013.

[34] A. Ephrath, Z. Eshcoli, and F. Berkowitz, "Probability of detection for $\mathcal{X}^2$ radar target in Weibull clutter," in *Proc. IEEE International Conference on Microwaves, Communications, Antennas and Electronic Systems (COMCAS)*, Tel Aviv, Israel, Nov 2011, pp. 1–5.

[35] A. Papoulis, *Probability, Random Variables, and Stochastic Processes*, 4th ed. New York: McGraw-Hill, 2002.

[36] W. Research, "DistributionFitTest," https://reference.wolfram.com/language/ref/DistributionFitTest.html, 2015.

[37] A. P. Prudnikov, Y. A. Bryčkov, and O. I. Maričev, *Integral and Series: Vol. 2*, 3rd ed., Fizmatlit, Ed. Moscow, Russia: Fizmatlit, 1992.

Appendix

APPENDIX A – CA-CFAR's property

To prove the non-dependence between λ^k and the PFA, we first expand the series in (2.29), that is,

$$P_{\text{FA}} = k^{N-1}\left(\frac{N}{\tau}\right)^{kN}\left(\frac{\delta_0\Gamma(N)}{\Gamma(kN)} + \frac{\delta_1\Gamma(N+1)\left(\frac{\lambda N}{\tau}\right)^k}{\Gamma(Nk+k)} + \frac{\delta_2\Gamma(N+2)\left(\frac{\lambda N}{\tau}\right)^{2k}}{\Gamma(Nk+2k)} + \frac{\delta_3\Gamma(N+3)\left(\frac{\lambda N}{\tau}\right)^{3k}}{\Gamma(Nk+3k)} + \mathcal{R}(i)\right), \tag{A.1}$$

where $\mathcal{R}(i)$ represents the remainder terms of the series.

For convenience, we rewrite the coefficients δ_i $(\forall i \geq 1)$ as follows

$$\delta_i = \frac{(-1)^i N\left(\frac{1}{\lambda}\right)^{ik}\Gamma(k)^{N-i}}{i!}\mathcal{F}(i), \tag{A.2}$$

where $\mathcal{F}(i)$ represents remainders factors that do not depend of λ.

Now, replacing (2.11) and (A.2) into (A.1), it yields

$$P_{\text{FA}} = k^{N-1}\left(\frac{N}{\tau}\right)^{kN}\left(\frac{\Gamma(k)^N\Gamma(N)}{\Gamma(kN)} - \frac{N\Gamma(k)^{N-1}\Gamma(N+1)\left(\frac{\lambda N}{\tau}\right)^k\left(\frac{1}{\lambda}\right)^k}{\Gamma(Nk+k)}\mathcal{F}(1) + \frac{2N\Gamma(k)^{N-2}\Gamma(N+2)\left(\frac{\lambda N}{\tau}\right)^{2k}\left(\frac{1}{\lambda}\right)^{2k}}{2\Gamma(Nk+2k)}\mathcal{F}(2) - \frac{3N\Gamma(k)^{N-3}\Gamma(N+3)\left(\frac{\lambda N}{\tau}\right)^{3k}\left(\frac{1}{\lambda}\right)^{3k}}{6\Gamma(Nk+3k)}\mathcal{F}(3) + \mathcal{R}_{\mathcal{F}}(i)\right), \tag{A.3}$$

where $\mathcal{R}_{\mathcal{F}}(i)$ represents the remainder terms of the series considering the factors $\mathcal{F}(i)$. Finally, from (A.3) it can be easily noticed that the factor λ^k vanishes completely, yielding in (2.31). This completes the proof.

APPENDIX B – Absolute convergence of (2.31)

Herein, we present the proof of the absolute convergence of (2.31). Eq. (2.31) is an absolutely convergent series if satisfies the following:

$$\sum_{i=0}^{\infty} \frac{\left(\frac{N}{\tau}\right)^{ik} \Gamma(i+N)}{\Gamma(ik+Nk)} |\psi_i| < \infty. \tag{B.1}$$

The factor $|\psi_i|$ can be bounded as

$$|\psi_i| \leq \frac{1}{i\Gamma(k)} \sum_{l=1}^{i} \frac{|\psi_{i-l}|\,|-i+lN+l|\,\Gamma(lk+k)}{l!}. \tag{B.2}$$

Since the relation $\Gamma(lk+k)/l!$ in (B.2) can behave as an increasing function if $k \geq 1$, or as a decreasing function if $0 < k < 1$, two bounds must be found for (2.31).

For the case of $k \geq 1$, we employ the fact that $1/\Gamma(k) < 2$ and that $|-i+lN+l| \leq iN$, $\forall 1 \leq l \leq i$. Thus, $|\psi_i|$ can be further bounded as

$$|\psi_i| < 2N \sum_{l=1}^{i} \frac{|\psi_{i-l}|\,\Gamma(lk+k)}{l!}. \tag{B.3}$$

Notice that (B.3) is an increasing function. Then, after using the last term of the sum and multiplying the resulting expression by i, it yields

$$\begin{aligned} |\psi_i| <& \frac{2N\psi_0\Gamma(ik+Nk)}{\Gamma(i)} \\ =& \frac{2N\Gamma(k)^N\Gamma(ik+Nk)}{\Gamma(i)}. \end{aligned} \tag{B.4}$$

Now, employing the bound (B.4) in (B.1), and after separating the first term of the sum, we have

$$\sum_{i=0}^{\infty} \frac{\left(\frac{N}{\tau}\right)^{ik} \Gamma(i+N)}{\Gamma(ik+Nk)} |\psi_i| = \frac{\Gamma(N)\Gamma(k)^N}{\Gamma(kN)} + 2N\Gamma(k)^N \sum_{i=1}^{\infty} \frac{\left(\frac{N}{\tau}\right)^{ik} \Gamma(i+N)}{\Gamma(i)}. \tag{B.5}$$

Finally, solving the infinite sum in (B.5) with the aid of [37, eq. (5.2.3.1)] and provided that $|N/\tau| < 1$, one attains

$$\sum_{i=0}^{\infty} \frac{\left(\frac{N}{\tau}\right)^{ik} \Gamma(i+N)}{\Gamma(ik+Nk)} |\psi_i| = \frac{\Gamma(N)\Gamma(k)^N}{\Gamma(kN)} + \Gamma(k)^N 2N^2\Gamma(N) \left(\frac{N}{\tau}\right)^k \left[1 - \left(\frac{N}{\tau}\right)^k\right]^{-(N+1)}. \tag{B.6}$$

Notice that the upper bound for (B.1) exist and is finite. Consequently, (2.31) converges absolutely for $k \geq 1$.

For the case of $0 < k < 1$, notice in (B.1) that as i increases, the gamma function $\Gamma(i+N)$ in the numerator increases much faster than $\Gamma(i+N)$ in the denominator, then it immediately follows that (B.1) diverges. Thus, (2.31) diverges for $0 < k < 1$.